



Line strengths of rovibrational and rotational transitions in the $X^2\Pi$ ground state of OH



James S.A. Brooke^{a,*1}, Peter F. Bernath^{a,b}, Colin M. Western^c,
Christopher Sneden^d, Melike Afşar^e, Gang Li^{f,2}, Iouli E. Gordon^f

^a Department of Chemistry, University of York, York, YO10 5DD, UK

^b Department of Chemistry & Biochemistry, Old Dominion University, 4541 Hampton Boulevard, Norfolk, VA 23529-0126, USA

^c School of Chemistry, University of Bristol, Cantock's Close, Bristol, BS8 1TS, UK

^d Department of Astronomy, University of Texas at Austin, Austin 78712, TX, USA

^e Department of Astronomy and Space Sciences, Ege University, 35100 Bornova, Izmir, Turkey

^f Harvard-Smithsonian Center for Astrophysics, Atomic and Molecular Physics Division, Cambridge 02138, MA, USA

ARTICLE INFO

Article history:

Received 23 March 2015

Received in revised form

27 July 2015

Accepted 28 July 2015

Available online 6 August 2015

Keywords:

OH hydroxyl radical

Line intensities

Einstein A values

Dipole moment function

Meinel system

Line lists

ABSTRACT

A new line list including positions and absolute transition strengths (in the form of Einstein A values and oscillator strengths) has been produced for the OH ground $X^2\Pi$ state rovibrational (Meinel system) and pure rotational transitions. All possible transitions are included with v' and v'' up to 13, and J up to between 9.5 and 59.5, depending on the band. An updated fit to determine molecular constants has been performed, which includes some new rotational data and a simultaneous fitting of all molecular constants. The absolute transition strengths are based on a new dipole moment function, which is a combination of two high level ab initio calculations. The calculations show good agreement with an experimental $v=1$ lifetime, experimental μ_v values, and $\Delta v=2$ line intensity ratios from an observed spectrum. To achieve this good agreement, an alteration in the method of converting matrix elements from Hund's case (b) to (a) was made. Partitions sums have been calculated using the new energy levels, for the temperature range 5–6000 K, which extends the previously available (in HITRAN) 70–3000 K range. The resulting absolute transition strengths have been used to calculate O abundances in the Sun, Arcturus, and two red giants in the Galactic open and globular clusters M67 and M71. Literature data based mainly on [O I] lines are available for the Sun and Arcturus, and excellent agreement is found.

© 2015 Elsevier Ltd. All rights reserved.

1. Introduction

The OH radical is very important in atmospheric chemistry due to its high reactivity with volatile organic compounds [1,2], and it is the major oxidizing species in the lower atmosphere [3]. OH is also produced in the

upper atmosphere in excited vibrational levels, and near infrared emission to lower levels is the main cause of the nighttime airglow of the upper atmosphere [4,5]. This airglow is often an unwanted feature in astronomical observations [6], but has sometimes been used for wavelength calibration [5] and atmospheric temperature retrievals [7]. OH is also present in stars [8], interstellar clouds [9], extra-terrestrial atmospheres [10,11], and often in relatively large concentrations [12] in flames [13–15].

The transitions of interest in this work are in the Meinel system, which are the rotational and rovibrational transitions within the $X^2\Pi$ ground state. These have been used to

* Corresponding author. Tel.: +44 1904 434525.

E-mail address: jsabrooke@gmail.com (J.S.A. Brooke).

¹ Now at: School of Chemistry, University of Leeds, Leeds, LS2 9JT, UK.

² Now at: Physikalisch-Technische Bundesanstalt (PTB), Bundesallee 100, 38116 Braunschweig, Germany.

determine the oxygen abundance in the Sun [16,17] and other stars, for example by Meléndez and Barbuy [18] and Smith et al. [19].

There have been several ab initio dipole moment functions (DMFs) calculated for the OH ground state [20–25]. Accurate experimental dipole moments were obtained for the $v=0, 1$, and 2 levels by Peterson et al. [26], and these were used by Nelson et al. [28,27] in combination with their own experimental relative line intensities to calculate a DMF at internuclear distances between 0.70 and 1.76 Å. Another experimental DMF was obtained by Turnbull and Lowe [29], also using the Peterson et al. values and their own experimental intensities. The various DMFs have all disagreed to some extent [27] (also see Fig. 1), including around the equilibrium internuclear distance (r_e), where the intensities are most sensitive to the DMF.

A set of absolute transition strengths was calculated by Mies [30], and more recently Goldman et al. [31] produced a set which is now the most widely used for abundance calculations, for example by Meléndez and Barbuy [18]. This list by Goldman et al. is currently in the HITRAN [32] database, and more extensively in the HITEMP [33] database. The values are based on the DMF of Nelson et al. [27] between 0.70 and 1.76 Å, and an unpublished DMF from Chackerian et al. at other internuclear distances. Another line list including ab initio Einstein A_{jj} values was calculated recently [24,25], however the accuracy can be improved, and it did not cover all of the available vibrational levels (up to $v=9$ as opposed to $v=13$). This DMF is included in the comparisons in Fig. 1.

Bernath and Colin [34] performed a fit to obtain molecular constants up to $v=13$ in 2009, using the best data available at the time. Lines from the extensive study of Mélen et al. [35] were included, along with the rovibrational measurements of Abrams et al. [15] (22 bands, $\Delta v=1\text{--}3$, up to $v=10$), Nizkorodov et al. [36] (11–9 band), and Sappey and Copeland [37] (12–8 band), and $B^2\Sigma^+ - X^2\Pi$ system lines from Copeland et al. [38] ($v=7\text{--}13$ in the $X^2\Pi$ state and $v=0\text{--}1$ in the $B^2\Sigma^+$ state). They also assigned new rotational lines in $v=4$ in an ATMOS (1994) [39] solar spectrum.

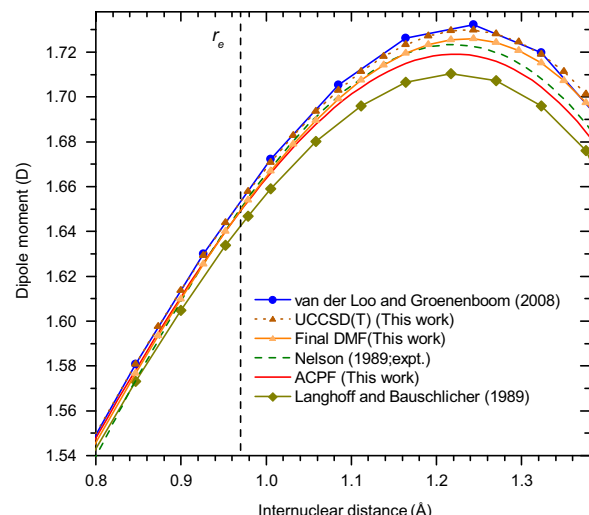


Fig. 1. Calculated and experimental dipole moment functions for the OH $X^2\Pi$ state.

The fit of Mélen et al. [35] included rotational lines in $v=0\text{--}3$, from both their assignments of an ATMOS (1985) [40] solar spectrum and laboratory measurements, and rovibrational laboratory data from Maillard et al. [13]. Hyperfine rotational data in $v=0\text{--}3$ from several other studies [41–59] were also included in the fit by Mélen et al. [35]. Despite hyperfine structure not being included in the results of Bernath and Colin [34], they took some of this information into account by adding pseudo-transitions to the fit, between e and f parity levels and various J levels (“ Λ -doubling data”), based on the term values calculated by Mélen et al. [35]. For a further description of the sources of the included transitions, the reader is referred to Table 1 of Bernath and Colin [34] and Fig. 4 of Mélen et al. [35].

Due to limitations in the fitting program used by Bernath and Colin [34], four separate fits were required to calculate all of the molecular constants. In addition, more rotational data in $v=0\text{--}2$ has recently been reported [60], which has a higher reported accuracy than the previously available lines. A fit in which this new data was included and all parameters were floated simultaneously was performed in this work, and is described in Section 2.

In this paper, the currently available HITRAN transition strengths are compared with experimental data (a $v=1$ lifetime [61], $\Delta v=2$ H–W ratios (this work), and μ_v values [26]). Based on these comparisons, it was concluded that the calculation of a new set of absolute transition strengths would be beneficial, and Sections 3–7 describe their calculation and validation. Partition function calculations are described in Section 8, and Section 9 uses the newly calculated transition strengths to calculate the O abundance in the Sun and three other stars, to demonstrate their use in astronomical calculations.

2. Molecular constant fit

A new fit of molecular constants was performed using PGOPHER, which sets up N^2 Hamiltonians, using the constants shown in Table 1, and performs a least-squares fit to a set of observed line positions. This fit was based mainly to that of Bernath and Colin [34]. Line weightings from the previous fit were retained, all parameters were floated simultaneously, and lines were replaced by new pure rotational data from Martin-Drumel et al. [60] where possible, which was the only new data included. The Λ -doubling data included by Bernath and Colin [34] was also included here, and as with their fit, no hyperfine structure constants were calculated. The PGOPHER observed line list input file is available in the Supplementary Material.

The fit of Bernath and Colin [34] was very extensive in terms of the number of molecular constants obtained. A number of higher order constants that had unreasonable fitting uncertainties were fixed at values based on extrapolation and careful inspection of the energy level patterns.

The same molecular constants as used by Bernath and Colin [34] were used here, and those that were fixed previously were also fixed. Floating these constants was attempted, but their resulting uncertainties were too large. As all parameters were now being floated, the uncertainties in general increased, and some of the higher order constants that were successfully determined in the fit of

Table 1

Molecular constants^a for the OH $X^2\Pi$ state (in cm^{-1}). The second and third columns show the maximum observed J values for each vibrational level (observed and reported in the line list).

Max. J								
v	Obs.	Rept.	T	A	B	$D \times 10^3$	$H \times 10^7$	$L \times 10^{11}$
0	50.5	60.5	0	-139.050877(41)	18.53487308(79)	1.9089352(64)	1.42658(14)	-1.4707(11)
1	42.5	50.5	3570.35244(72)	-139.32031(62)	17.82391990(96)	1.870447(10)	1.37737(33)	-1.5700(35)
2	41.5	50.5	6975.09355(69)	-139.58940(54)	17.1224805(18)	1.835828(12)	1.31875(33)	-1.6991(41)
3	39.5	45.5	10,216.1478(12)	-139.84424(86)	16.427914(26)	1.80599(16)	1.2447(37)	-1.824(32)
4	32.5	40.5	13,294.6144(14)	-140.0832(17)	15.737018(34)	1.78267(21)	1.1630(37)	-2.124(19)
5	19.5	25.5	16,210.5997(18)	-140.2893(19)	15.045630(63)	1.76640(58)	0.9956(143)	[-1.416]
6	18.5	25.5	18,962.9921(19)	-140.4396(23)	14.348665(68)	1.76159(67)	0.8425(176)	[-1.75]
7	18.5	25.5	21,549.1777(19)	-140.5041(19)	13.639345(70)	1.77073(73)	0.6013(204)	[-1.74]
8	12.5	20.5	23,964.6390(21)	-140.4296(16)	12.90888(12)	1.8002(18)	0.3214(773)	[-3.4]
9	13.5	20.5	26,202.4452(19)	-140.1409(16)	12.145349(64)	1.85782(47)	[-0.111]	[-5.8]
10	11.5	15.5	28,252.5370(31)	-139.5064(17)	11.33258(17)	1.9571(20)	[-0.717]	[-12.5]
11	8.5	15.5	30,100.8094(29)	-138.3238(17)	10.45025(33)	2.1383(85)	[-1.5]	...
12	7.5	12.5	31,728.2544(35)	-136.3625(19)	9.45859(52)	2.349(13)	[-2.5]	...
13	7.5	13.5	33,109.6605(30)	-133.0318(23)	8.32780(25)	2.7906(46)	[-4.0]	...
v	$M \times 10^{15}$	$N \times 10^{20}$	$O \times 10^{23}$	$\gamma \times 10$	$\gamma_D \times 10^5$	$\gamma_H \times 10^9$	$\gamma_L \times 10^{13}$	$q \times 10^2$
0	0.8842(25)	[6.2]	[-3.96]	-1.19251(14)	2.357(13)	-3.021(218)	3.47(103)	-3.86908(17)
1	1.258(11)	[-8.80]	[-4.0]	-1.13749(54)	2.315(18)	-2.467(282)	[3.5]	-3.69357(18)
2	1.721(14)	[-32.6]	[-4.0]	-1.07690(48)	2.192(15)	-1.523(228)	[3.5]	-3.51941(29)
3	2.007(92)	[-66.0]	[-4.0]	-1.0250(32)	2.353(159)	-1.96(111)	[3.5]	-3.3393(21)
4	[2.5]	[-100]	[-4.0]	-0.9664(42)	2.473(274)	-3.14(252)	[3.5]	-3.1590(33)
5	[2.8]	[-100]	...	-0.9035(46)	2.591(266)	[-6.4]	...	-2.9719(40)
6	[3.1]	[-100]	...	-0.8390(56)	3.191(361)	[-17.1]	...	-2.7800(45)
7	[3.4]	[-100]	...	-0.7593(51)	3.240(362)	[-17.7]	...	-2.5781(49)
8	[3.7]	[-100]	...	-0.6744(63)	4.353(576)	[-30.0]	...	-2.3593(75)
9	[4.0]	[-100]	...	-0.5558(64)	5.313(648)	[-60]	...	-2.1184(82)
10	[4.3]	[-100]	...	-0.4010(85)	[6.0]	[-100]	...	-1.861(29)
11	-0.2981(190)	[7.0]	-1.564(68)
12	0.4404(207)	[8.5]	-1.284(31)
13	0.8677(115)	[10.0]	-0.7239(207)
v	$q_D \times 10^5$	$q_H \times 10^9$	$q_L \times 10^{13}$	$q_M \times 10^{17}$	p	$p_D \times 10^5$	$p_H \times 10^9$	$p_L \times 10^{12}$
0	1.4739(14)	-2.713(29)	4.358(225)	-3.42(26)	0.235355(20)	-5.216(21)	5.635(380)	-1.050(194)
1	1.4451(14)	-2.591(32)	3.961(133)	[-2.08] ^b	0.224684(30)	-5.235(27)	7.775(529)	[-2.88] ^b
2	1.4342(15)	-2.786(29)	5.180(125)	[-2.0]	0.213190(81)	-5.003(30)	4.386(460)	[-3.20] ^b
3	1.403(13)	-2.505(201)	4.748(886)	[-2.0]	0.20276(35)	-5.310(233)	6.54(191)	[-3.0]
4	1.400(19)	-2.484(137)	[4.79] ^b	[-2.0]	0.19120(43)	-5.296(260)	[3.80] ^b	[-3.0]
5	1.388(21)	[-2.5]	0.17937(59)	-5.701(438)	[3.5]	...
6	1.413(26)	[-2.75] ^b	0.16642(59)	-5.949(485)	[2.8]	...
7	1.427(30)	[-2.69] ^b	0.15223(63)	-6.479(566)	[1.8]	...
8	1.464(66)	[-3.0]	0.13578(86)	-7.111(957)	[1.0]	...
9	1.475(79)	[-3.3]	0.11694(88)	-8.29(116)
10	1.612(394)	[-3.6]	0.09316(231)	-8.96(459)
11	[1.7] ^b	0.04981(193)	[-12,000]
12	[1.8] ^b	0.03033(168)	[-18,000]
13	[1.9] ^b	-0.05720(168)	[-27,000]

^a Constants in square brackets were fixed; one standard deviation in the last digits is given in parentheses; the constants with their full precision as used by PGOPHER are available in the Supplementary Material.

^b Fixed here at the value from Bernath and Colin [34], but floated in their fit.

Bernath and Colin [34] were fixed at their previous values. Compared to the work of Bernath and Colin [34], the small amount of new data and simultaneous determination of all constants resulted in only a small improvement in the fit. Specifically, the total unweighted average line position error changed from 0.02649 to 0.02637 cm^{-1} , and the weighted average error improved by a factor of 1.32.

See Table 1 for the final molecular constants. These are available with more precision in the PGOPHER input file in the Supplementary Material.

3. Kitt Peak experimental spectrum and Herman–Wallis ratios

Relative intensities were extracted from an experimental FTS spectrum from Abrams et al. [15], for later comparison with our calculated values. The spectrum was recorded at the Kitt Peak National Observatory, Arizona, by observing OH emission from the $\text{H} + \text{O}_3$ reaction, and it has an excellent signal-to-noise ratio. The intensity axis of the observed spectrum was calibrated using a NIST traceable tungsten

ribbon filament lamp (Optronics Model 550C), a spectrum of which had been recorded using the same equipment. The $\Delta v=2$ region was chosen for analysis as the OH lines are strongest here, it is the cleanest region (mostly due to the presence of water lines in the $\Delta v=1$ region), and the calibration curve is much flatter in the $\Delta v=2$ region. Lines were fitted using WSPECTRA [62], the areas were taken as the intensities, and Herman–Wallis (H–W) ratios (described below) were obtained for bands up to 9–7.

OH contains a light H atom, and so exhibits a strong H–W effect [63], meaning that the line intensity heavily depends on J . The obvious effect on the spectrum is that the P branches are more intense than the R branches. When comparing calculated intensities to an observed spectrum, this effect can be exploited to validate the line parameters. The intensity ratio of an R branch line to a P branch line with the same upper J level will vary with J , and as the same upper (for an emission spectrum) J level is used, the effects on intensity due to energy level population are canceled. This intensity ratio is hereafter referred to as the H–W ratio. The intensities obtained are available in the Supplementary Material.

4. Absolute transition strength calculation method

4.1. Einstein A values

Absolute transition strengths are reported in this paper as Einstein A values ($A_{JJ'}$) and oscillator strengths ($f_{JJ'}$), which can be calculated using the following equations:

$$A_{JJ'} = \frac{16\pi^3\nu^3 S_{JJ'}}{3\epsilon_0 hc^3(2J'+1)} \quad (1)$$

$$= 3.136\ 188\ 94 \times 10^{-7} \frac{\tilde{\nu}^3 S_{JJ'}}{(2J'+1)} \quad (2)$$

$$f_{JJ'} = \frac{m_e e_0 c}{2\pi e^2 \nu^2} \frac{(2J'+1)}{(2J+1)} A_{JJ'} \quad (3)$$

$$= 1.499\ 1938 \frac{1}{\tilde{\nu}^2} \frac{(2J'+1)}{(2J+1)} A_{JJ'}, \quad (4)$$

where $A_{JJ'}$ is in s^{-1} , $\tilde{\nu}$ is in wavenumbers, and $S_{JJ'}$ is the line strength in debye squared, equal to the square of the transition matrix element (ME), $\langle \psi' | \hat{\mu} | \psi \rangle$, summed over the degenerate upper and lower M_J levels. These MEs can be calculated using the program PGOPHER using a Hund's case (a) basis set. PGOPHER accomplishes this by setting up case (a) Hamiltonians as described in Section 2, and case (a) transition matrices containing the MEs of the space fixed electric dipole operator, $T_p^k(\mu)$ (in spherical tensor notation):

$$\langle \eta' \Lambda' v' ; S\Sigma' ; J' \Omega' | T_p^k(\mu) | \eta \Lambda v ; S\Sigma ; J \Omega \rangle, \quad (5)$$

where η represents the remaining electronic quantum numbers, k is the rank of the tensor (equal to 1 for single photon transitions), and p is the component in the laboratory frame. In PGOPHER the Hamiltonians are diagonalized, and the resulting eigenvectors are combined with the case (a) MEs to give transformed transition matrices, which contain the required MEs, $\langle \psi' | \hat{\mu} | \psi \rangle$. This accounts for the mixed Hund's case (a)/(b) character of the state.

The following sections describe the calculation of the case (a) transition MEs in Eq. (5).

4.2. Calculation of Hund's case (a) matrix elements

$T_p^k(\mu)$ (Eq. (5)) is conventionally expanded [64] in terms of a molecule fixed dipole moment operator, $T_q^k(\mu)$, and a Wigner D matrix, $D_{p,q}^k(\omega)$, that gives the transformation between the space and molecule fixed axis systems:

$$T_p^k(\mu) = \sum_q D_{p,q}^k(\omega)^* T_q^k(\mu). \quad (6)$$

In a Hund's case (a) basis the wavefunctions can be expressed as a product of a rotational part, $|JM\Omega\rangle$, and a vibronic part, $|\eta\Lambda v; S\Sigma\rangle$. Taking matrix elements of the dipole operator, the standard approach yields a product of terms:

$$\begin{aligned} & \sum_q \langle J'M'\Omega' | D_{p,q}^k(\omega)^* | JM\Omega \rangle \\ & \times \langle \eta' \Lambda' v' ; S\Sigma' | T_q^k(\mu) | \eta \Lambda v ; S\Sigma \rangle \delta_{S'S} \delta_{\Sigma\Sigma}, \end{aligned} \quad (7)$$

with the first term containing integrals over the rotational wavefunctions leading to Hönl-London factors and the second term, the vibronic transition moment being a band strength independent of rotation. The delta functions arise as the electric dipole operator does not act on electron spin. To allow for case (a)/(b) mixing the standard methods will give rotational wavefunctions that are linear combinations of the basis functions, $|JM\Omega\rangle|\eta\Lambda v; S\Sigma\rangle$, giving slightly more complicated expressions.

Given a potential energy curve for an electronic state, $V_{\eta\Lambda}(r)$, derived as described in Section 4.3, the vibrational wavefunctions, $\Psi_{\eta\Lambda v}(r)$, can be calculated by solving the one dimensional Schrödinger equation ignoring the effect of electron spin and framework rotation):

$$-\frac{\hbar^2}{2\mu} \frac{d^2\Psi_{\eta\Lambda v}(r)}{dr^2} + V_{\eta\Lambda}(r) \Psi_{\eta\Lambda v}(r) = E_{\eta\Lambda v} \Psi_{\eta\Lambda v}(r), \quad (8)$$

The vibronic transition moment is then evaluated by integrating the DMF, $\mu_{\eta\Lambda}(r)$ over the vibrational wavefunctions involved:

$$\langle \eta' \Lambda' v' | T_q^k(\mu) | \eta \Lambda v \rangle = \int_0^\infty \Psi_{\eta\Lambda v}(r) \mu_{\eta\Lambda}(r) \Psi_{\eta\Lambda v}(r) dr \quad (9)$$

The H–W effect arises because the vibrational wavefunctions change with rotation, which can be modeled by adding a centrifugal term:

$$\frac{\hbar^2}{2\mu r^2} (N(N+1) - \Lambda^2) = B(r) (N(N+1) - \Lambda^2) \quad (10)$$

to the potential energy in the Schrödinger equation above. A separate vibrational wavefunction, $\Psi_{\eta\Lambda v,N}(r)$ then arises for each value of N , and the formally vibronic transition moment acquires a variation with N . To reflect this we add additional labels to the transition moment:

$$\langle \eta' \Lambda' v' | T_q^k(\mu; N'N) | \eta \Lambda v \rangle = \int_0^\infty \Psi_{\eta\Lambda v,N}(r) \mu_{\eta\Lambda}(r) \Psi_{\eta\Lambda v,N}(r) dr \quad (11)$$

This means that the Schrödinger equation must be solved separately for each value of N . The notation we have chosen is potentially confusing, as we have included the

additional quantum numbers in the operator, $T_q^k(\mu; N'N)$, rather than writing the matrix element as $\langle \eta'\Lambda'v'; N' | T_q^k(\mu) | \eta\Lambda v; N \rangle$. This choice emphasizes the N dependence introduced to the standard theory, and the fact that the wavefunctions $\Psi_{\eta\Lambda v, N}(r)$ are still essentially vibronic, as being body fixed, they do not contain the angles relating the space and body fixed axes.

There are two approaches to taking the spin into account. In the method described by Chackerian et al. [65], that has been used by Goldman et al. [31] to prepare the line list used in HITRAN 2012, a pair of coupled differential equations are set up, one for $\Omega = 1/2$ and one for $\Omega = 3/2$. This essentially corresponds to a Hund's case (a) basis. The diagonal terms are the one-dimensional Schrödinger equation as above, with the centrifugal term becoming $B(r)(J(J+1) - \Omega^2)$, and the addition of a constant spin-orbit coupling term, $A\Lambda\Sigma = \pm A/2$. The spin-orbit coupling constant, A , was assumed independent of r . This is an approximation, though Table 1 indicates a relatively small variation of A with v and thus r . The term mixing the $\Omega = 3/2$ to $\Omega = 1/2$ equations is $-B(r)\sqrt{J(J+1) - \Omega\Omega'}$, analogous to the $-B\hat{J}_+\hat{S}_-$ term normally used to model case (a)/(b) mixing ("spin uncoupling"). Solving the pair of equations gives a vibrational wavefunction for each v , J , and Ω , and the vibronic part of the transition moment is then evaluated by integrating the DMF over each pair of wavefunctions on the assumption that it is independent of Ω .

We use a simplified approach here, allowing us to use LeRoy's LEVEL program to solve a single differential equation (Eq. (8)) above with the rotational term from Eq. (10)) added, and ignore the electron spin in finding the vibrational wavefunctions. The dipole moment for a given N is then found by integrating the dipole moment over the spin independent wavefunction.

The two approaches will give different results; the most obvious change is that the effective case (a)/(b) mixing term calculated by PGOPHER will use an average value of B , rather than an operator that depends on r . We expect the differences to be small, and we were able to verify this with some partial calculations based on the alternate approach. LEVEL was modified to calculate the centrifugal term with half integral values of the electronic angular momentum, and wavefunctions calculated from our potential for selected values of v , J and Ω , and the $\Omega = 3/2$ to $1/2$ ME then evaluated by numerical integration of $-B(r)\sqrt{J(J+1) - \Omega\Omega'}$ over the resulting wavefunctions. To allow a direct comparison, a PGOPHER calculation was set up with a set of rotational constants B , D , H , L and M derived by fitting to the $\Lambda = 1$ eigenvalues from LEVEL, and excluding the lambda doubling and spin terms. Turning spin on in PGOPHER and comparing the resulting 2×2 case (a) Hamiltonian matrices with the $\Omega = 1/2$ and $3/2$ eigenvalues and the $\Omega = 1/2$ to $3/2$ ME calculated by numerical integration yielded very small differences. Even at $J = 49.5$ the MEs, energy differences and resulting coefficients were typically differing in the fifth significant figure only. This is much less than the accuracy we can claim for the dipole moment, so the approximation is good, and the remaining work used the unmodified version of LEVEL.

Integrating the dipole moment over wavefunctions, $\Psi_{\eta\Lambda v, N}(r)$, as above then gives essentially vibronic transition moments in a case (b) basis, which must be

transformed to a case (a) basis for use by PGOPHER as it always uses a case (a) basis. The required transformation has been derived and used in our previous papers, but it became clear as part of this work that a small but important correction to this is required, so we now summarise the revised derivation of this.

The transformation between case (a) functions, defined in terms of $\Omega = \Lambda + \Sigma$, and case (b) functions, defined in terms of N , is [66]:

$$\begin{aligned} & \langle \eta v \Lambda; N \Delta S J M \rangle \\ &= \sum_{\Sigma} (-1)^{N-S+\Lambda+\Sigma} \sqrt{2N+1} \begin{pmatrix} J & S & N \\ \Lambda+\Sigma & -\Sigma & -\Lambda \end{pmatrix} \\ & \quad \times | \eta v \Lambda; S \Sigma; J M \Omega \rangle. \end{aligned} \quad (12)$$

This allows any given case (a) ME to be expressed in terms of case (b) MEs:

$$\begin{aligned} & \langle \eta' v' \Lambda' S \Sigma' J' M' \Omega' | \hat{H} | \eta v \Lambda; S \Sigma; J M \Omega \rangle \\ &= \sum_{N'N} (-1)^{N'-N+S'-S+\Omega'-\Omega} \sqrt{(2N'+1)(2N+1)} \begin{pmatrix} J' & S' & N' \\ \Omega' & -\Sigma' & -\Lambda' \end{pmatrix} \\ & \quad \times \begin{pmatrix} J & S & N \\ \Omega & -\Sigma & -\Lambda \end{pmatrix} \langle \eta' v' \Lambda' S \Sigma' J M | \hat{H} | \eta v \Lambda; N \Delta S J M \rangle. \end{aligned} \quad (13)$$

The MEs of the transition dipole moment given in Eq. (7) above in a Hund's case (a) basis are

$$\begin{aligned} & \langle \eta' v' \Lambda' S \Sigma' J' M' \Omega' | T_p^k(\mu) | \eta v \Lambda; S \Sigma; J M \Omega \rangle = \sum_q (-1)^{M'-\Omega'} \\ & \quad \times \sqrt{(2J'+1)(2J+1)} \begin{pmatrix} J' & k & J \\ -\Omega' & q & \Omega \end{pmatrix} \begin{pmatrix} J' & k & J \\ -M' & p & M \end{pmatrix} \\ & \quad \times \langle \eta' v' \Lambda' S \Sigma' | T_q^k(\mu; J' \Omega' J \Omega) | \eta v \Lambda; S \Sigma \rangle. \end{aligned} \quad (14)$$

and in a Hund's case (b) basis:

$$\begin{aligned} & \langle \eta' v' \Lambda; N' S' J' M' | T_p^k(\mu) | \eta v \Lambda; N S J M \rangle = (-1)^{J'-M'} \\ & \quad \times \begin{pmatrix} J' & k & J \\ -M' & p & M \end{pmatrix} (-1)^{N'+S+J+k} \sqrt{(2J'+1)(2J+1)} \\ & \quad \times \begin{Bmatrix} N' & J' & S \\ J & N & k \end{Bmatrix} \sum_q (-1)^{N'-\Lambda'} \sqrt{(2N'+1)(2N+1)} \\ & \quad \times \begin{pmatrix} N' & k & N \\ -\Lambda' & q & \Lambda \end{pmatrix} \langle \eta' v' \Lambda' | T_q^k(\mu; N'N) | \eta v \Lambda \rangle. \end{aligned} \quad (15)$$

$\langle \eta' v' \Lambda' | T_q^k(\mu; N'N) | \eta v \Lambda \rangle$ is the quantity calculated by LEVEL. Combining the last three equations allows the Hund's case (a) and Hund's case (b) vibronic MEs to be related:

$$\begin{aligned} & \langle \eta' v' \Lambda' S \Sigma' | T_{\Omega'-\Omega}^k(\mu; J' \Omega' J \Omega) | \eta v \Lambda; S \Sigma \rangle \\ &= (-1)^{J'-\Omega'} \begin{pmatrix} J' & k & J \\ -\Omega' & \Omega'-\Omega & \Omega \end{pmatrix}^{-1} \sum_{N,N'} (-1)^{N'-N+\Omega'-\Omega+S+J+\Lambda'+k} \\ & \quad \times (2N'+1)(2N+1) \begin{pmatrix} J' & S & N' \\ \Omega' & -\Sigma' & -\Lambda' \end{pmatrix} \begin{pmatrix} J & S & N \\ \Omega & -\Sigma & -\Lambda \end{pmatrix} \\ & \quad \times \begin{Bmatrix} N' & J' & S \\ J & N & k \end{Bmatrix} \begin{Bmatrix} N' & k & N \\ -\Lambda' & \Lambda'-\Lambda & \Lambda \end{Bmatrix} \\ & \quad \times \langle \eta' v' \Lambda' | T_{\Lambda'-\Lambda}^k(\mu; N'N) | \eta v \Lambda \rangle. \end{aligned} \quad (16)$$

Note that the effective vibronic transition moment, $\langle \eta' \Lambda' | T_{\Lambda'-\Lambda}^k (\mu; J' N') | \eta \Lambda \rangle$, depends on both J and Ω . A more complete derivation is given in the Supplementary Material. The key difference from the previous version [67] is the removal of the condition that $\Omega = \Omega'$, and in the OH case this results in MEs in a Hund's case (a) basis with $\Delta\Omega = \pm 1$ in addition to the normal $\Delta\Omega = 0$ MEs. That this is a direct consequence of the N (or J) dependence of the vibronic transition moment follows from the result (shown in the Supplementary Material) that if the vibronic transition moment is independent of N the expected result follows:

$$\begin{aligned} & \langle \eta' \Lambda' | T_{\Lambda'-\Lambda}^k (\mu; N' N) | \eta \Lambda \rangle \\ &= \langle \eta' \Lambda' | S' \Sigma' | T_{\Omega'-\Omega}^k (\mu; J' \Omega' J \Omega) | \eta \Lambda; S \Sigma \rangle \delta_{\Sigma' \Sigma} \delta_{S' S}, \end{aligned} \quad (17)$$

and the vibronic transition moment is independent of J and has the selection rule $\Delta\Omega = \Delta\Lambda$ (or $\Delta\Sigma = 0$).

The H–W effect therefore has the effect of introducing small MEs off-diagonal in Ω in the case (a) basis. For example, for the (2, 0), R(1.5) transition, the transition matrix changes as shown in Table 2. Note that this is in the Hund's case (a) basis; after diagonalization all four MEs will always be non-zero for this state.

4.3. Potential energy curve

Equilibrium constants (Table 3) were calculated by least-squares fitting to Eqs. (18) and (19), using the

Table 2

Symmetrised e transition matrix in a Hund's case (a) basis for the (2, 0), R(1.5) example transition. Upper - with original transformation equation. Lower - including $\Delta\Sigma \neq 0$ MEs. The quantum numbers $v'=2, v=0, J'=2.5$, and $J=1.5$ are omitted for clarity. The top rows contain the upper states, and the left column the lower states. All values are in debye.

	${}^2\Pi_{(1.5)}(e/f)$	${}^2\Pi_{(0.5)}(e/f)$
${}^2\Pi_{(1.5)}(e/f)$	−0.01157	0
${}^2\Pi_{(0.5)}(e/f)$	0	−0.01418
	${}^2\Pi_{(1.5)}(e/f)$	${}^2\Pi_{(0.5)}(e/f)$
${}^2\Pi_{(1.5)}(e/f)$	−0.01157	−0.0002774
${}^2\Pi_{(0.5)}(e/f)$	−0.0001114	−0.01418

Table 3

Equilibrium molecular constants (in cm^{-1}) for the OH $X^2\Pi$ state. These constants with the full precision used in the calculations are available in the Online Supplementary Material.

Constant ^a	Value	Constant	Value
ω_e	3738.465(19)	B_e	18.894867(49)
$\omega_e x_e$	84.875(18)	α_{e_1}	0.72343(15)
$\omega_e y_e$	0.5409(77)	α_{e_2}	0.007212(138)
$\omega_e z_e$	−0.02252(170)	α_{e_3}	−0.0006656(469)
$\omega_e \eta_{e_1}$	−0.0009854(1986)	α_{e_4}	0.00005108(598)
$\omega_e \eta_{e_2}$	0.00003087(1155)	α_{e_5}	−0.000004828(251)
$\omega_e \eta_{e_3}$	−0.000004539(264)		

^a Numbers in parentheses indicate one standard deviation in units of the last significant digits of the constants.

constants T_v and B_v from Table 1:

$$\begin{aligned} G_v = & \omega_e \left(v + \frac{1}{2} \right) - \omega_e x_e \left(v + \frac{1}{2} \right)^2 + \omega_e y_e \left(v + \frac{1}{2} \right)^3 + \omega_e z_e \left(v + \frac{1}{2} \right)^4 \\ & + \omega_e \eta_{e_1} \left(v + \frac{1}{2} \right)^5 + \omega_e \eta_{e_2} \left(v + \frac{1}{2} \right)^6 + \omega_e \eta_{e_3} \left(v + \frac{1}{2} \right)^7, \end{aligned} \quad (18)$$

$$\begin{aligned} B_v = & B_e - \alpha_{e_1} \left(v + \frac{1}{2} \right) + \alpha_{e_2} \left(v + \frac{1}{2} \right)^2 + \alpha_{e_3} \left(v + \frac{1}{2} \right)^3 \\ & + \alpha_{e_4} \left(v + \frac{1}{2} \right)^4 + \alpha_{e_5} \left(v + \frac{1}{2} \right)^5 \end{aligned} \quad (19)$$

These were employed in the program `RKR1` [68] which can generate a potential energy curve using the first-order semiclassical Rydberg–Klein–Rees procedure [69–72]. This potential energy curve is available in the online Supplementary Material (in the `LEVEL` output file).

4.4. Comparison to HITRAN calculations

To show that the results obtained using this adjusted transformation equation are reasonably equivalent to the potentially more accurate HITRAN style calculation involving separate vibrational wavefunctions for each Ω component, calculations were performed using a DMF equivalent to that used for HITRAN, and also the HITRAN molecular constants. The DMF was constructed using the Nelson et al. [27] DMF at short range (the same range as used for HITRAN), and our ACPF DMF (Section 5) at long range (as the long range part used for HITRAN does not appear to have been published). This means that compared to the actual DMF used for HITRAN, it is identical at short range, but then diverges slightly. Hereafter, it is referred to as the “HITRAN DMF”.

Fig. 2 plots the ratio of the Einstein A values obtained using both the revised and original transformation methods, and the HITRAN DMF and molecular constants. Much better agreement is seen with the use of the revised transformation method. As the potential used in this comparison is not exactly that used for HITRAN, some of the discrepancies are due to this small difference. Transitions are only shown up to $v' = 2$ as the potential and DMF will begin to diverge from those of HITRAN at higher v levels.

The improvement in the transformation method is further demonstrated in Fig. 3, which compares the H–W ratios obtained using both transformation methods and the HITRAN DMF, with those of HITRAN. With the use of the revised transformation equation, the calculated values reproduce the HITRAN results almost exactly.

Fig. 3 also shows the observed ratios, which were obtained as described in Section 3. Note the splitting of the solid (F_{11} transitions) and dotted (F_{22} transitions) lines of the same color. This splitting is caused by the distribution of intensity between the F_{11} and F_{22} transitions. The splitting pattern obtained from HITRAN and using the revised transformation equation agrees with that of the observed lines, although the calculated lines are displaced upwards on the graph from the observed lines. This is caused by inaccuracies in the DMF, and the next section describes a

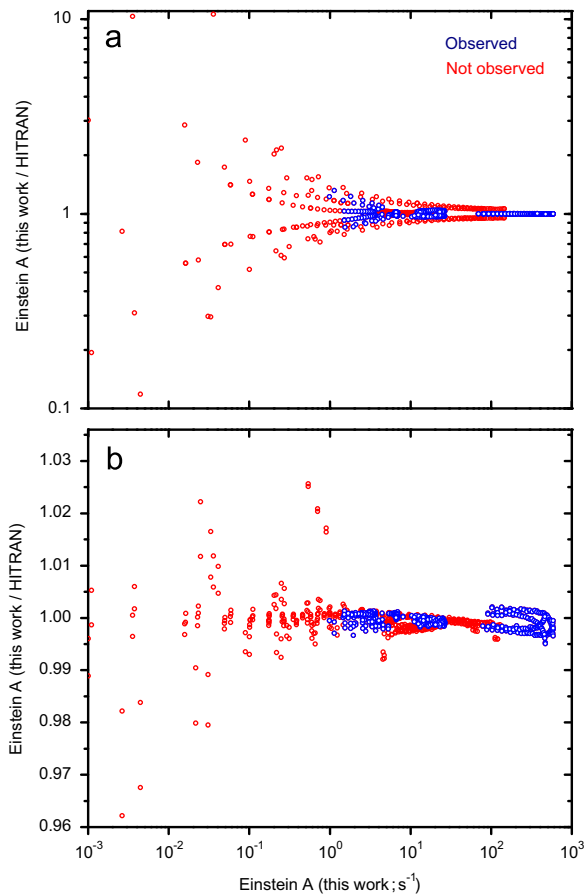


Fig. 2. Ratio of Einstein A values between HITRAN and those obtained from using the methods described in this work but with the HITRAN 2012 molecular constants and DMF. (a) Using the previous version of the transformation equation. (b) Using the final version of the transformation equation. Transitions are shown for all bands (including pure rotational) with v' up to 2, and where $F' = F'$. “Observed” means that the transitions have been identified in experimental spectra, but does not refer to observed intensities.

new DMF, the calculation of which is aimed at obtaining better agreement with experimental measurements.

5. Dipole moment functions

5.1. Final DMF and ab initio calculations

A new DMF was used in this work, which is a combination of two ab initio DMFs. At large internuclear distances, an averaged coupled-pair functional (ACPF) [73–76] DMF was used, and at small distances, an unrestricted open shell coupled-cluster method with single, double, and perturbative triple excitations (UCCSD(T)) [77] DMF was used.

The ACPF DMF was calculated using MOLPRO 2012.1 [78], using an aug-cc-pV6Z basis set [79–81]. This followed a complete active space self-consistent field (CASSCF) [82,83] calculation using an active space of four σ , four π , and one δ orbital. The UCCSD(T) DMF was calculated with MOLPRO 2010.1 [77], and with the aug-cc-pV6Z basis set

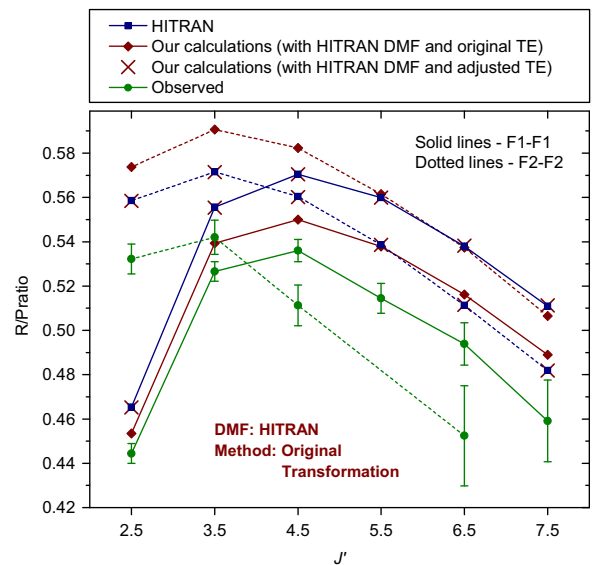


Fig. 3. H–W ratios in the OH $X^2\Pi$ (2, 0) band. The values plotted are equal to the R branch intensity divided by the P branch intensity for transitions that share an upper J and F level (an average of two parity transitions). The red lines are calculated using our methods (but the previous version of the transformation equation) and potential, and the HITRAN DMF and molecular constants.

[79–81]. For both DMFs, all core correlations were included, and the dipole moments were calculated by the finite field method.

A comparison of these DMFs and others is shown in Fig. 1. A full description of the mixing of the two DMFs to produce the final version is provided in Section 5.3.

5.2. Results from using only ab initio DMFs

The full calculations were performed using both ab initio DMFs individually, and the results were analysed by comparison to the experimental dipole moments of Peterson et al. [26], an experimental lifetime obtained recently by van de Meerakker et al. [61], and H–W ratios.

Better agreement with the Peterson et al. [26] dipole moments was shown with the ACPF DMF than any of the other DMFs shown, except for that of Nelson et al., which is expected as the Nelson et al. DMF is partly based on these experimental measurements. This is shown in Fig. 4, where it can also be seen that the UCCSD(T) DMF does not agree as well.

The lifetime of the $v=1$ level was calculated as the weighted (for e and f parity levels) sum of the Einstein A values for all possible transitions from a single upper J level ($J=1.5, F_1$), and taking the reciprocal. Unfortunately, the result for the ACPF potential of 65.36 ms does not fall within the error bounds of the recent experimental measurement. The UCCSD(T) DMF produces a lifetime in excellent agreement of 59.14 ms. Lifetimes were also calculated using our methods, potential, and line positions, but using the other literature DMFs. All of these are shown in Table 4, which shows that the UCCSD(T) lifetime is the best match to the experimental value.

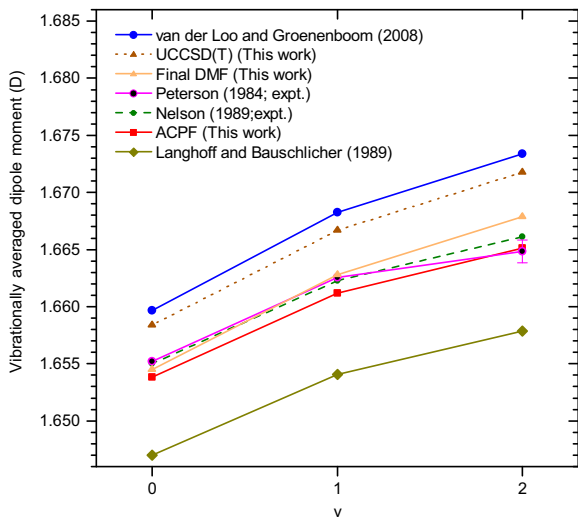


Fig. 4. Calculated and experimental μ_v values of OH ($X^2\Pi$). The error bars of the experimental values for $v=0$ and $v=1$ are not shown as they are slightly smaller than the size of the symbols.

Table 4

Calculated and experimental lifetimes of the OH $X^2\Pi$, $v=1, J=1.5, F_1$ level, using different DMFs. The first column is the literature source of the DMF. The second is the lifetime reported in that paper, and the third is the lifetime calculated using the specified DMF, but with our methods, potential, and line positions.

DMF	Lifetime (ms)	
	Reported by authors	Calculated in this work
van de Meerakker et al. [61] (expt.)	59 ± 2	...
van der Loo and Groenenboom [24,25]	56.84	56.97
Langhoff et al. [23]	73.3	66.7
HITRAN 2012 [32]	$56.6 \pm 10\text{--}20\%$	56.6
This work (ACPF DMF)	...	65.36
This work (UCCSD(T) DMF)	...	59.14
This work (Final DMF; UCCSD(T)+ACPF)	...	59.13

H–W ratios calculated from the Kitt Peak spectrum as described in Section 3 were obtained for $\Delta v=2$ bands up to (9, 7), and compared to our calculated values and those of HITRAN. Results from the two DMFs are quite similar for the low vibrational bands, and are closer to the observed ratios than HITRAN. For the higher vibrational bands, the calculated ratios show worse agreement with the observed ratios for the UCCSD(T) DMF than the ACPF DMF.

5.3. Mixing of ab initio DMFs to form final DMF

The $v=1$ lifetime is determined mainly by the gradient of the DMF around R_e , and as can be seen in Fig. 1, this varies between the various DMFs that have been calculated. The shape of the DMF also determines the magnitude of the H–W effect, and as the UCCSD(T) DMF reproduces these well, its shape is likely to be accurate.

The match to the experimental μ_v values can be improved by subtracting a constant from the DMF, whilst retaining its shape. The single-reference UCCSD(T) method does not perform well at longer range (in this case above about 2.1 Å). Therefore, it was decided to use the UCCSD(T) at short range, the ACPF at long range, and to mix them in the intermediate region.

The best intermediate region that gave a resulting DMF with smooth first and second derivatives was found to be 1.5–2.1 Å. To achieve this, a value was added to the ACPF DMF. To ensure that the ACPF still decreased smoothly to zero, this value was smoothly decreased to zero with increasing range.

Specifically, the ACPF DMF was split into three regions, one where the full amount was added ($r < 1.5$ Å), one where the amount added was smoothly decreased to zero ($1.5 \text{ \AA} < r < 3.0 \text{ \AA}$), and one where nothing was added ($r > 3.0 \text{ \AA}$). The amount added in the smoothing region was equal to

$$a \frac{1}{2} \left(\cos \left(\frac{1.5}{\pi} (r - 1.5) \right) + 1 \right), \quad (20)$$

where a is the maximum amount added.

In the mixing region, the final DMF is a linear combination of the two adjusted ab initio DMFs:

$$\text{DMF} = c(\text{ACPF}) + (1 - c)(\text{UCCSD(T)}), \quad (21)$$

where the coefficient c is equal to

$$\frac{1}{2} \left(\cos \left(\frac{0.6}{\pi} (r - 1.5) \right) + 1 \right). \quad (22)$$

A fit of the DMF was performed, in which the final intensities were fitted to the $\Delta v=2$ H–W ratios (from 100 upper J levels in the 2–0 to 9–7 bands) and the Peterson et al. [26] μ_v values, and the parameters floated were the maximum value added to the ACPF DMF (0.04988 D), and the value subtracted from the UCCSD(T) DMF (0.001534 D). The μ_v values were weighted such that their weights were proportional to the reciprocal of their reported uncertainties, and the sum of their weights was equal to the sum of the weights of all of the H–W ratio data. The H–W ratios were weighted using the reciprocal of their uncertainties (calculated as described in Section 3). The $v=1$ lifetime was not used in the fit, as all of the floated parameters have a negligible effect on it, and it is already reproduced well by the DMF. The mixing of the two DMFs using the final parameters is shown in Fig. 5, and the DMFs are all available in the Supplementary Material.

5.4. Comparison to Nelson et al. [27] fit

Nelson et al. [27] calculated their DMF by fitting an expansion about R_e to three sets of experimental values: the three Peterson et al. [26] μ_v values, about 70 $\Delta v=1$ H–W ratios from their own experimental spectrum, and $\Delta v=2$ to $\Delta v=1$ ratios for nine upper J levels. The uncertainties of their $\Delta v=1$ H–W ratios were larger than for our $\Delta v=2$ H–W ratios, possibly partly due to the $\Delta v=2$ region being much less contaminated by other lines. For the lower vibrational bands, our calculated $\Delta v=1$ H–W ratios

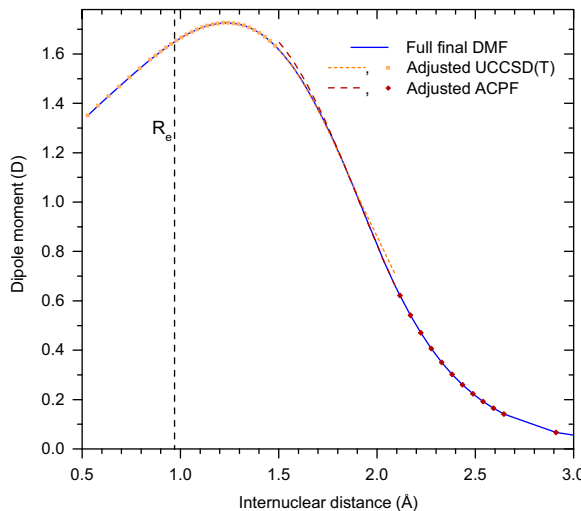


Fig. 5. Mixing of the two *ab initio* DMFs to form a final DMF.

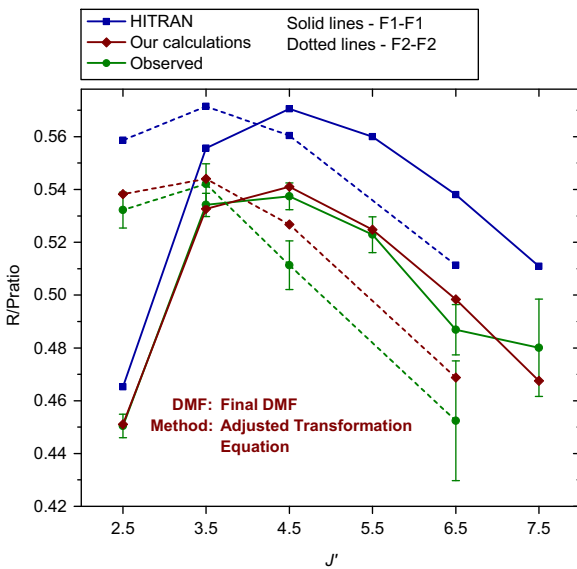


Fig. 6. Observed and calculated H–W effect in the OH $X^2\Pi$, (2, 0) band, using the final DMF and calculation method. See Fig. 3 for full description.

match their observed values about as well as theirs do. These differences increase for the higher vibrational bands, but the overall weighted root mean square error using our calculated Einstein A values compared to those of HITRAN is only 1.41 times higher (for F_{11}), and 1.22 (for F_{22}). For comparison, for the $\Delta v=2$ H–W ratios, these errors are 3.27 and 4.02 times higher using the HITRAN Einstein A values compared to using ours.

A figure equivalent to Fig. 3 was produced using the final data (Fig. 6), which shows a good match to the observed H–W ratios. Our calculated lifetime (59.13 ms) is also much closer to the experimental measurement of van de Meerakker et al. [61] than that calculated using the HITRAN DMF (56.6 ms; Table 4). Figures for the 3–1 to 9–7

bands also show good agreement with the observed ratios, and these are available in the Supplementary Material in Figure S1.

6. Final line list and comparisons

A line list was produced for all possible rovibrational and rotational transitions within the $X^2\Pi$ state, for v up to 13, and J up to between 9.5 and 59.5, depending on the band. Transitions are reported between J levels that are a few higher than those observed for each vibrational level. The maximum J values observed and reported are shown in Table 1.

A comparison of the final Einstein A values and those of HITRAN is shown in Fig. 7. The top panel shows all the F_1 – F_1 and F_2 – F_2 transitions. There are 277 (out of about 17 000) transitions with a ratio of more than 10 or less than 0.1 that do not appear in the figure. It is expected that for any new calculation of this kind, the extremely weak transitions will be so sensitive to any changes in

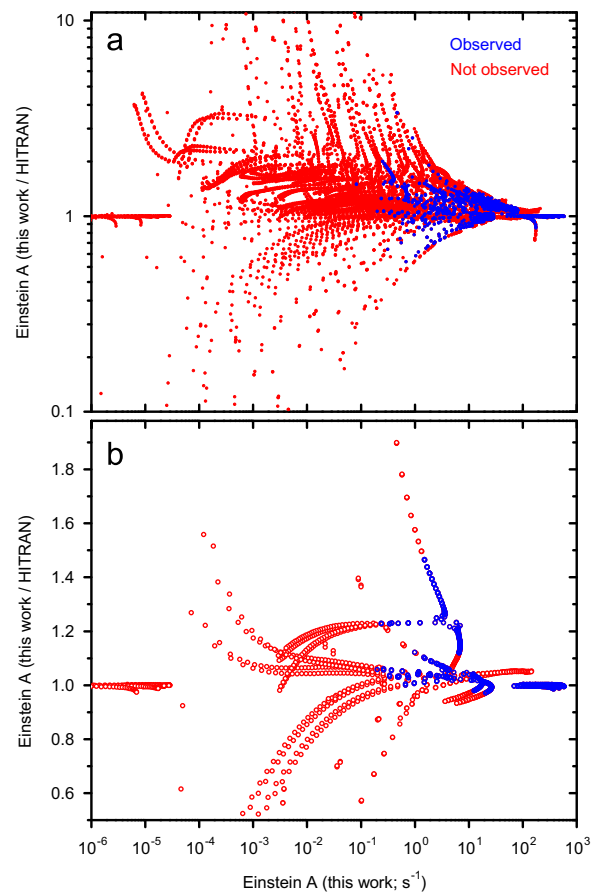


Fig. 7. Ratio of Einstein A values between HITRAN and those from this work. (a) All vibrational bands. (b) All bands (including pure rotational) with v' up to 2. For both panels, the transitions shown are F_1 – F_1 and F_2 – F_2 only. “Observed” means that the transitions have been identified in experimental spectra, but does not refer to observed intensities.

parameters, that such ratios of several orders of magnitude will be seen. This only applies to transitions that are unlikely to ever be observed.

The lower panel shows transitions with v' up to 2 so as to be comparable with Fig. 2b. The differences for the stronger transitions in Fig. 7b are not large, but they are still much larger than the differences in Fig. 2b. This means that the differences in transition strengths between this and the previous study are mainly due to the DMF, and not the different calculation method.

The difference in the satellite transitions is slightly more than the main transitions. A comparison is shown in Fig. 8. There are about 2400 transitions that lie outside of the y -axis bounds in this figure, but the scale is kept the same so as to be comparable to Fig. 7b. The general trend for most of the stronger transitions is that Einstein A values have been increased by a factor of between 1 and 1.5. The change for the satellite transitions shows the same trend, which further validates the calculation method, as their values will be very sensitive to changes in off-diagonal MEs.

Ref. [31] discusses sensitive cases and anomalies in the line intensities. These occur when wavefunctions almost completely cancel, so that the resulting overlap and therefore transition strength is extremely sensitive to changes in any of the parameters. This has been observed previously [84,85], and means that these sensitivities are unimportant as they only occur for very weak transitions that are unlikely to ever be observed. Goldman et al. [31] pointed out a specific case; the $(1, 0), ^5R_{21}$ (4.5) line. In this work, the anomalies will not be the same, as we do not directly calculate the wavefunctions and overlap separately for the different spin-components. In a plot of Einstein A against J'' for the $(1, 0), ^5R_{21}$ branch, the $J'' = 4.5$ Einstein A is simply located at the minimum, about an order of magnitude lower than the peaks at $J'' = 1.5$ and 11.5.

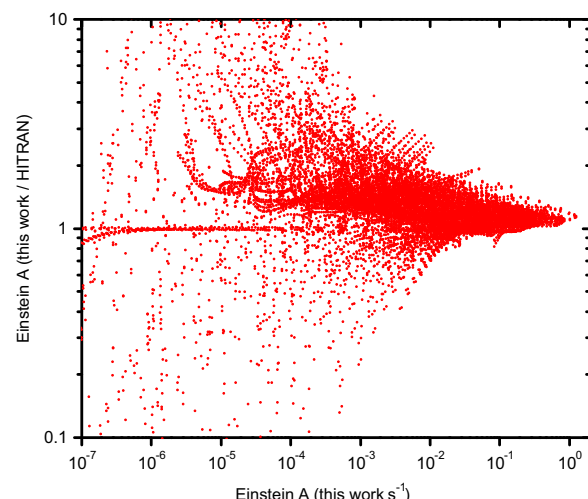


Fig. 8. Ratio of Einstein A values between HITRAN and those from this work for F_1-F_2 transitions.

Table 5
Vibrational lifetimes of the OH $X^2\Pi$ state.

v	Lifetime (ms)
1	59.13
2	31.20
3	21.40
4	16.07
5	12.54
6	10.01
7	8.12
8	6.75
9	5.77
10	5.11
11	4.76
12	4.73
13	5.16

7. Lifetimes and band strengths

Vibrational lifetimes were calculated for all of the v levels observed, and are shown in Table 5.

A_{vv} values have been calculated for all reported vibrational bands, and these are available in the Online Supplementary Material. They are calculated by summing over the Einstein A_{jj} values for all possible transitions from $J' = 1.5$, F_1 , for each band. The A_{vv} values have also been converted into vibrational band oscillator strengths (f_{vv} -values) using the following equation [86]:

$$f_{vv} = 1.499\ 1938 \frac{1}{\tilde{\nu}^2} \frac{(2 - \delta_{0,\Lambda'})}{(2 - \delta_{0,\Lambda})} A_{vv}, \quad (23)$$

where $\Lambda' = \Lambda = 1$.

8. Partition function

The partition sums currently provided with the HITRAN database are those from the TIPS2011 code described by Laraia et al. [87]. The values are given between 70 and 3000 K. Considering that OH is observed in both very cold and very hot environments, we decided to extend this range to 5–6000 K. As we now have an extended number of calculated energy levels, we calculated the partition function using direct summation over the levels derived in Section 2. Our values agree well with those calculated using TIPS2011 and those provided in the JPL spectroscopic catalogue (based on Ref. [88]).

The hydrogen $I=1/2$ hyperfine structure is taken into account simply by including a twofold degeneracy for each level, consistent with the approach taken by HITRAN. As the hyperfine splitting is very small, this makes a negligible difference to the calculated values. Fig. 9 shows the relative differences between partition sums calculated here, and those calculated using TIPS2011 and through direct summation of the energy levels given in the JPL database (which include hyperfine splitting for every level). In general there is good agreement; the discrepancy at low J is an artefact of the interpolation scheme used in TIPS2011, which is based on values tabulated at 25 K intervals. The growing divergence from the JPL values at higher temperatures appears because the JPL catalogue includes only first three vibrational levels. However, in this

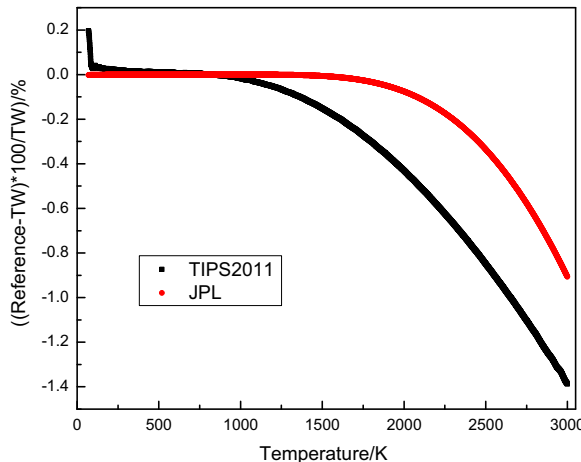


Fig. 9. Relative differences between the partition sums calculated in this work, and those calculated using TIPS2011 and through direct summation of the energy levels given in the JPL database. TW stands for “this work”.

work we now provide the data between 5 and 6000 K, which is a significant and important extension to the previously available partition sums. The list of partition sums is given in the Supplementary Material.

9. OH and the oxygen abundances of the Sun and stars

9.1. General remarks

OH rovibrational bands can be important features for determination of oxygen abundances in cool stars (those with effective temperatures $T_{\text{eff}} \leq 5500$ K). They can be attractive alternatives to the visible-region 6300, 6363 Å [O I] red lines, which are often weak and blended with other atomic/molecular transitions, and to the 7770 Å high-excitation O I triplet lines, whose strengths are subject to significant departures from local thermodynamic equilibrium (LTE). Here we report preliminary oxygen abundance analyses from OH lines for a handful of stars, and compare our results to published abundances in the literature.

We applied the new OH rovibrational line list to high-resolution spectra of the Sun and three cool giant stars in the 1.5–1.8 μm wavelength region (the astronomical photometric *H* band). Many lines of the Δv=2 system occur in the *H* band, but a large fraction of them are blended with transitions of neutral atomic species, and especially with molecular CN and CO bands. Therefore for the present exploratory analysis we limited our line list in this spectral region to 15 relatively clean transitions used in a pioneering study of the Δv=2 band system [89].

Several large telescopes now have instruments capable of obtaining high resolution ($R \equiv \lambda/\Delta\lambda = 20,000$ –80,000), high signal-to-noise (S/N) *H*-band spectra, e.g. VLT CRIRES [90], SDSS APOGEE [91], and newly-commissioned McDonald IGRINS [92]. These facilities will yield a rich set of cool stars with easily detectable OH lines. The four stars chosen for analysis here represent different temperatures,

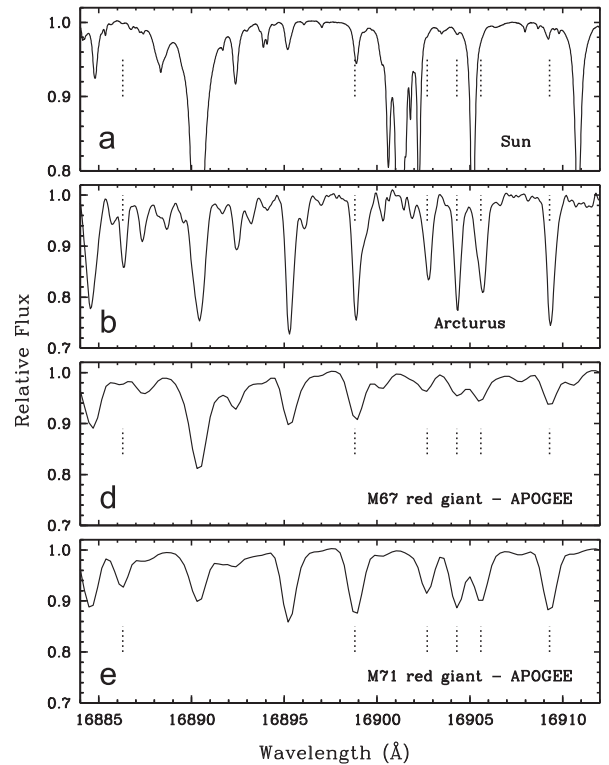


Fig. 10. Observed spectra of the four program stars in the wavelength interval covered by Fig. 1 in Ref. [89]. Vertical dotted lines denote wavelengths of the OH lines. Telluric lines have been removed from the stellar spectra (panels b–e) but not from the solar photospheric spectrum (panel a).

gravities, metallicities and Galactic population memberships, and they have published oxygen abundances. These stars offer differing challenges for OH analyses. In Fig. 10 we display a small spectral interval in each of our program stars. This wavelength range was chosen to match that in Fig. 1 of Meléndez [89]. The OH lines are strong in Arcturus and the cool giants of M67 and M71, but are challenging to detect in the other stars.

Lines of the OH Δv=1 system have been studied as part of a comprehensive investigation of the solar oxygen abundance [93]. The Δv=1 lines are much stronger than the Δv=2 ones, but they occur in the 3–4 μm spectral domain (the photometric *L* band). This bandpass is difficult to access with ground-based high-resolution spectroscopy because the thermal background is higher and the telluric H₂O absorption is more time-variable in the *L* band than in the *H* band. It is challenging to construct efficient high-resolution spectrographs for the *L* band. Therefore relatively few chemical composition studies have featured *L*-band data. However, high-quality spectra are available for the Sun and the mildly metal-poor giant Arcturus, and we have applied the new line lists to Δv=1 lines in these two stars.

In Section 9.2 we describe the analyses of each star in turn. Standard stellar spectroscopic notation is employed here: (a) the “absolute” abundances of a given element *A*

in a star is defined as $\log \epsilon(A) = \log(N_A/N_H) + 12.0$; (b) the relative abundance ratio of elements A and B with respect to their solar ratio is written as $[A/B] = \log(N_A/N_B)_\odot - \log(N_A/N_B)_\odot$; and (c), metallicity will be taken to be the $[\text{Fe}/\text{H}]$ value.

9.2. Abundances in individual stars

9.2.1. The solar photosphere

We employed the 15 lines given in Table 1 of Meléndez [89] but did not adopt their equivalent widths (EW) for our solar OH analysis. These lines are all extremely weak: $0.7 \text{ m}\AA \leq \text{EW} \leq 1.4 \text{ m}\AA$, with $\langle \text{EW} \rangle \approx 1.1 \text{ m}\AA = 1.1 \times 10^{-7} \mu\text{m}$. This translates to a mean reduced width of $\langle RW \rangle = \langle \text{EW} \rangle / \lambda \approx -7.2$. Such lines are at the limit of reliable EW measurement, and given the potential for contamination by other solar photospheric and telluric absorptions, we opted to derive an oxygen abundance for each line by matching synthetic and observed spectra. Our analyses followed closely those of previous papers in this series on MgH [94], C₂ [95], and CN [96]; here we briefly summarize those methods.

We synthesized a small spectral range, usually 12 Å, surrounding each OH line, using the LTE stellar spectrum analysis code MOOG [97].³ Assembly of the synthesis transition list began with the atomic linedatabase of Kurucz [98], adding or updating the line parameters of atomic species that have had recent lab analyses by the Wisconsin atomic physics group ([99] and references therein for Fe-group elements; [100] and references therein for neutron-capture elements). Molecular transitions of CO [98], CN [96] and OH [this study] were merged with the atomic data. Since these line lists were also to be applied to the spectra of giant evolved stars, we include the major CNO isotopologues: ¹²CN, ¹³CN, ¹²CO, and ¹³CO.

For the solar analysis we adopted the photospheric abundances recommended by Asplund et al. [101], in particular $\log \epsilon(\text{C})=8.43$, $\log \epsilon(\text{N})=7.83$, $\log \epsilon(\text{O})=8.69$, and $^{12}\text{C}/^{13}\text{C}=89$. To maintain consistency with previous papers in this series, we used the empirical model photosphere of Holweger and Müller [102]. Model atmosphere parameters for the Sun and all other stars are given in Table 6. The observed spectrum was that obtained by L. Delbouille, G. Brault, J.W. Brault, and L. Testerman at Kitt Peak National Observatory.⁴ With the model, line list and observed spectrum inputs we created synthetic spectra and altered the oxygen abundance until best synthesis/observation matches were obtained. Results for each line and the mean abundance statistics are listed in Table 7.

Our OH solar photospheric oxygen abundance, $\log \epsilon(\text{O})=8.72$, is only 0.03 dex larger than that recommended by Asplund et al. [101] from multiple oxygen-containing species (significantly weighted by the [O I] 6300 Å transition). Given the extreme weakness of the OH $\Delta v=2$ solar lines, we regard the offset as negligible. We also examined the photospheric *L*-band spectrum, finding a few very weak and unblended OH $\Delta v=1$ transitions. From these

we estimate $\langle \log(\epsilon(\text{O})) \rangle \approx 8.75$, in reasonable agreement with the results from the $\Delta v=2$ transitions.

9.2.2. Thick disk red giant Arcturus

The very bright mildly metal-poor star Arcturus has been studied many times at high spectral resolution. Our recent study of the CN red and violet systems [96] featured Arcturus; that paper gives references to previous analyses. Its OH lines are strong (panel (b) of Fig. 10) and straightforward to analyze. We used model atmosphere parameters derived by Ram et al. [95] to generate synthetic spectra, and compared them to the Arcturus spectral atlas [103]. The resulting mean O abundance (Table 6) of $\log \epsilon = 8.68$ translates to a relative overabundance of $[\text{O}/\text{Fe}] = +0.51$. This value is slightly larger than that derived from the [O I] lines by Sneden et al. [96], but is in excellent accord with that derived by Ram et al. [95].

9.2.3. Red giants in galactic open and globular clusters

Members of star clusters are tempting targets for chemical composition studies since their atmospheric parameters T_{eff} and $\log g$ can often be reliably estimated simply by broad-band photometry. APOGEE⁵ [104] is a dedicated high-resolution spectroscopic survey of more than 100,000 stars in the *H* band. The APOGEE instrument covers most of the *H* band at a resolving power of $R=20,000$, and currently is producing publicly-available spectra for both field and cluster red giant targets. From a list kindly supplied by Gail Zasowsky, we acquired APOGEE spectra of solar-metallicity old open cluster M67 star 2M08490674+1129529, and mildly metal-poor globular cluster M71 star 2M19533986+1843530. The APOGEE database⁶ gives derived atmospheric quantities for these stars that we adopt here (Table 6). These stars do not have previously published O abundances, but the values derived here are consistent with expectations for their clusters: (a) $[\text{O}/\text{Fe}] \approx 0.0$ for the metal-rich M67, and (b) $[\text{O}/\text{Fe}] \approx +0.5$ for the lower-metallicity M71. Detailed comparison of O abundances from OH and [O I] features should be done in the future, along with derivation of O abundances in all APOGEE targets in as many clusters as possible.

In summary, the new OH line lists reported in this paper yield O abundances that are in excellent agreement with those determined from visible spectral region features. The Einstein *A* values used in these calculations are around 13% lower than in HITRAN, which translates to a $\log(gf)$ change of -0.06 (from HITRAN to this work). If the calculations were performed with the HITRAN values, the resulting abundances would therefore be approximately 0.06 dex lower. For the Sun, this would result in $\log \epsilon(\text{O})=8.66$, in equally good agreement with the recommended values as our result. The HITRAN value for Arcturus would be $\log \epsilon(\text{O})=8.66$, equal to the value shown in Table 6 (calculated by Sneden et al. [96]), but our value is in better agreement with another recently calculated value (8.76 ± 0.17 ; reported by Ramírez and Allende Prieto [105]).

⁵ APOGEE: The Apache Point Observatory Galactic Evolution Experiment; see <http://www.sdss3.org/surveys/apogee.php>.

⁶ <http://data.sdss3.org/bulkIRSpestra/apogeeID>.

³ Available at <http://www.as.utexas.edu/~chris/moog.html>.

⁴ Available at http://bass2000.obspm.fr/solar_spect.php.

Table 6

Stellar model parameters and abundance summary.

Star	T_{eff} (K)	$\log(g)$	v_{micro} (km s $^{-1}$)	[Fe/H]	$\log \epsilon(\text{C})$ adopted	$\log \epsilon(\text{N})$ adopted	$\log \epsilon(\text{O})$ [O I]	$\log \epsilon(\text{O})$ OH	[O/Fe] [O I]	[O/Fe] OH
Sun	5780	4.44	0.85	0.00	8.43	7.83	8.69	8.72	+0.00	+0.03
Arcturus	4286	1.66	2.00	-0.52	8.02	7.66	8.62	8.68	+0.45	+0.51
M67 ^a	4623	2.44	1.62	+0.06	8.38	7.94	...	8.78	...	+0.03
M71 ^b	4314	1.48	2.00	-0.77	(7.36)	(7.06)	...	8.44	...	+0.52

^a star 2M08490674+1129529 in open cluster M6.^b star 2M19533986+1843530 in globular cluster M71.**Table 7**

Parameters and O abundances from individual OH lines.

λ (μm)	χ (eV)	$\log(gf)$	Sun ^a (km s $^{-1}$)	Arcturus	M67 ^b	M71 ^c
1.52785	0.205	-5.435	...	8.72	8.76	8.46
1.54091	0.255	-5.435	8.74	8.72	8.76	8.44
1.55687	0.299	-5.337	8.74	8.67	8.78	8.45
1.60527	0.639	-4.976	8.79	8.69	8.82	8.44
1.61921	0.688	-4.957	8.79	8.69	8.75	8.44
1.63681	0.730	-4.858	8.74	8.65	...	8.48
1.64560	0.609	-5.108	8.69	8.68
1.65345	0.781	-4.806	8.59	8.67	...	8.42
1.66054	0.981	-4.816	8.69	8.67	8.77	8.42
1.66559	0.681	-5.069	...	8.70	8.83	8.47
1.68722	0.759	-5.032	8.69	...	8.78	8.42
1.68862	1.059	-4.720	8.74	8.62	8.75	8.41
1.69042	0.896	-4.712	...	8.66	8.75	8.45
1.69092	0.897	-4.712	...	8.69	8.80	8.45
1.76189 ^d	1.243	-4.454
Mean		8.72	8.68	8.78	8.44	
+/-		0.02	0.01	0.01	0.01	
Sigma		0.06	0.03	0.03	0.02	
# lines		10	13	11	13	

^a All abundances are in units of $\log \epsilon$.^b star 2M08490674+1129529 in open cluster M67.^c star 2M19533986+1843530 in globular cluster M71.^d 1.76189 μm from Ref. [89] was unable to be used in any of our program stars, but is listed here for completeness.

Preliminary analyses of OH lines appearing in new high-resolution IGRINS [92] spectra of several evolved stars have also shown better matches to previous abundances for our values than those of HITRAN.

10. Summary and conclusion

New absolute transition strengths have been calculated for the OH Meinel system that we believe to be the most accurate available. The absolute transition strengths in common use are based on a DMF from 1990 [27], and using the newly calculated UCCSD(T)/ACPF mixed DMF, a better match to an experimental lifetime [61] and $\Delta v=2$ H–W ratios is observed. Similarly good agreement is seen with the experimental μ_v values, but slightly worse agreement with the $\Delta v=1$ H–W ratios observed by Nelson et al. [27]. The new line list includes transitions for v up to 13, and J up to between 9.5 and 59.5, depending on the band, and is available in the Online Supplementary Material.

The “transformation equation”, that converts transition MEs from Hund’s case (b) to (a) (and between LEVEL and PGOPHER) was changed to include $\Delta \Sigma \neq 0$ MEs. For molecules with a small H–W effect, the effect of this change is very small. It is important when the H–W effect is large such as for OH, but also for NH, for which we recently published a list of transition strengths [67]. The NH list has been updated with the use of this adjusted method [106].

Partition sums have been calculated using the energy levels obtained in this work, and are available in the Online Supplementary Material. They cover the temperature range 5–6000 K, which is an increased range compared to what was previously available in HITRAN (70–3000 K). This will enable the calculation of line intensities in cold environments such as interstellar clouds, and hot environments such as stars.

The absolute transition strengths for 15 $\Delta v=2$ transitions have been used to calculate O abundances in the Sun and three other stars, which are compared to abundances recommended in the literature where available. The OH-based O abundances for the Sun and Arcturus are in agreement with the values derived from the [O I] 6300 Å lines, and those for the two cluster targets are consistent with their expected O abundances. Additionally, our preliminary analyses of OH lines appearing in new high-resolution IGRINS [92] spectra of several evolved stars, including an extremely metal-deficient star, yield very reliable O abundances.

The visible spectral region [O I] lines can be difficult to work with in many stars, due to contamination by other atomic/molecular stellar features and by telluric O₂ absorption and night-sky [O I] emission. Given good high-resolution H-band spectra, the OH lines in some cases will easily be able to serve as the primary O abundance indicators, particularly for target stars that are heavily reddened.

The line list produced in this work will be useful in the fields of atmospheric science, astronomy, and combustion science.

Acknowledgements

Support for this work was provided by a Research Project Grant from the Leverhulme Trust and the Department of Chemistry (University of York) studentship. Some support was also provided by the NASA Origins of Solar Systems program. M.A. was supported by the Turkish

Scientific and Technological Research Council (TÜBİTAK, Project 112T929). We are grateful to Gail Zasowski for assistance with the APOGEE database. Thanks also go to Jeremy J. Harrison for helpful discussions about the transformation equation.

Appendix A. Supplementary data

Supplementary data associated with this paper can be found in the online version at <http://dx.doi.org/10.1016/j.jqsrt.2015.07.021>.

References

- [1] Atkinson R, Arey J. Atmospheric degradation of volatile organic compounds. *Chem Rev* 2003;103(12):4605–38. <http://dx.doi.org/10.1021/cr0206420>.
- [2] Lelieveld J, Dentener FJ, Peters W, Krol MC. On the role of hydroxyl radicals in the self-cleansing capacity of the troposphere. *Atmos Chem Phys* 2004;4:2337–44.
- [3] Prinn RG, Weiss RF, Miller BR, Huang J, Alyea FN, Cunnold DM, et al. Atmospheric trends and lifetime of CH_3CCl_3 and global OH concentrations. *Science* 1995;269:187–92. <http://dx.doi.org/10.1126/science.269.5221.187>.
- [4] Meinel TAB. OH emission bands in the spectrum of the night sky. *Astrophys J* 1950;111:555. <http://dx.doi.org/10.1086/145296>.
- [5] Oliva E, Origlia L. The OH airglow spectrum – a calibration source for infrared spectrometers. *Astron Astrophys* 1992;254:466.
- [6] Maihara T, Iwamuro F, Yamashita T, Hall DNB, Cowie LL, Tokunaga AT, et al. Observations of the OH airglow emission. *Astro Soc Pac* 1993;105:940–4.
- [7] Sivjee GG, Hamwey RM. Temperature and chemistry of the polar mesopause OH. *J Geophys Res* 1987;92:4663–72. <http://dx.doi.org/10.1029/JA092iA05p04663>.
- [8] Wilson WJ, Schwartz PR, Neugebauer G, Harvey PM, Becklin EE. Infrared stars with strong 1665/1667-MHz OH microwave emission. *Astrophys J* 1972; 177:523. <http://dx.doi.org/10.1086/151729>.
- [9] Heiles CE. Normal OH emission and interstellar dust clouds. *Astrophys J* 1968;151:919. <http://dx.doi.org/10.1086/149493>.
- [10] Piccioni G, Drossart P, Zasova L, Migliorini A, Gérard JC, Mills FP, Virtis-Venus Express Technical Team Collaboration, et al. First detection of hydroxyl in the atmosphere of Venus. *Astron Astrophys* 2008; 483: L29–33. <http://dx.doi.org/10.1051/0004-6361:200809761>.
- [11] Atreya SK, Gu ZG. Stability of the Martian atmosphere: is heterogeneous catalysis essential? *J Geophys Res* 1994; 99(E6): 13133–45. <http://dx.doi.org/10.1029/94JE01085>.
- [12] Settersten TB, Farrow RL, Gray JA. Infrared ultraviolet double-resonance spectroscopy of OH in a flame. *Chem Phys Lett* 2003;369: 584–90. [http://dx.doi.org/10.1016/S0009-2614\(03\)00022-8](http://dx.doi.org/10.1016/S0009-2614(03)00022-8).
- [13] Maillard JP, Chauville J, Mantz AW. High-resolution emission spectrum of OH in an oxyacetylene flame from 3.7 to 0.9 μm . *J Mol Spectrosc* 1976;63:120–41. [http://dx.doi.org/10.1016/0022-2852\(67\)90139-7](http://dx.doi.org/10.1016/0022-2852(67)90139-7).
- [14] Ewart P, O'Leary SV. Detection of OH in a flame by degenerate four-wave mixing. *Opt Lett* 1986;11:279–81. <http://dx.doi.org/10.1364/OL.11.000279>.
- [15] Abrams MC, Davis SP, Rao MLP, Engleman Jr R, Brault JW. High-resolution Fourier transform spectroscopy of the Meinel system of OH. *Astrophys J Suppl* 1994;93:351–95. <http://dx.doi.org/10.1086/192058>.
- [16] Grevesse N, Sauval AJ, van Dishoeck EF. An analysis of vibration-rotation lines of OH in the solar infrared spectrum. *Astron Astrophys* 1984;141:10–6.
- [17] Goldman A, Murcay DG, Lambert DL, Dominy JF. The pure rotation spectrum of the hydroxyl radical and the solar oxygen abundance. *Mon Not R Astron Soc* 1983;203:767–76.
- [18] Meléndez J, Barbuy B. Keck NIRSPEC infrared OH lines: oxygen abundances in metal-poor stars down to $[\text{Fe}/\text{H}] = -2.9$. *Astrophys J* 2002;575:474–83. <http://dx.doi.org/10.1086/341142>.
- [19] Smith VV, Cunha K, Shetrone MD, Meszaros S, Allende Prieto C, Bizyaev D, et al. Chemical abundances in field red giants from high-resolution H-band spectra using the APOGEE spectral linelist. *Astrophys J* 2013;765:16. <http://dx.doi.org/10.1088/0004-637X/765/1/16>.
- [20] Stevens WJ, Das G, Wahl AC, Krauss M, Neumann D. Study of the ground state potential curve and dipole moment of OH by the method of optimized valence configurations. *J Chem Phys* 1974;61: 3686–99. <http://dx.doi.org/10.1063/1.1682554>.
- [21] Werner HJ, Rosmus P, Reinsch EA. Molecular properties from MCSCF-SCEP wave functions. I. Accurate dipole moment functions of OH, OH^- , and OH^+ . *J Chem Phys* 1983;79:905–16. <http://dx.doi.org/10.1063/1.445867>.
- [22] Langhoff SR, Werner HJ, Rosmus P. Theoretical transition probabilities for the OH Meinel system. *J Mol Spectrosc* 1986;118: 507–29. [http://dx.doi.org/10.1016/0022-2852\(86\)90186-4](http://dx.doi.org/10.1016/0022-2852(86)90186-4).
- [23] Langhoff SR, Bauschlicher CW, Taylor PR. Theoretical study of the dipole moment function of OH ($X^2\Pi$). *J Chem Phys* 1989;91(10): 5953–9. <http://dx.doi.org/10.1063/1.457413>.
- [24] van der Loo MPJ, Groenenboom GC. Theoretical transition probabilities for the OH Meinel system. *J Chem Phys* 2007;126(11): 114314. <http://dx.doi.org/10.1063/1.2646859>.
- [25] van der Loo MPJ, Groenenboom GC. Erratum: theoretical transition probabilities for the OH Meinel system (J Chem Phys 2007; 126: 114314). *J Chem Phys* 2008; 128(15): 159902. <http://dx.doi.org/10.1063/1.2899016>.
- [26] Peterson KL, Fraser GT, Klemperer W. Electric dipole moment of $X^2\Pi$ OH and OD in several vibrational states. *Can J Phys* 1984;62(12):1502–7. <http://dx.doi.org/10.1139/p84-196>.
- [27] Nelson DD, Schiffman A, Nesbitt DJ, Orlando JJ, Burkholder JB. $\text{H}+\text{O}_3$ Fourier-transform infrared emission and laser absorption studies of OH ($X^2\Pi$) radical: an experimental dipole moment function and state-to-state Einstein A coefficients. *J Chem Phys* 1990;93(10):7003–19. <http://dx.doi.org/10.1063/1.459476>.
- [28] Nelson Jr DD, Schiffman A, Nesbitt DJ, Yaron DJ. Absolute infrared transition moments for open shell diatomics from J dependence of transition intensities – application to OH. *J Chem Phys* 1989;90: 5443–54. <http://dx.doi.org/10.1063/1.456450>.
- [29] Turnbull DN, Lowe RP. An empirical determination of the dipole moment function of OH ($X^2\Pi$). *J Chem Phys* 1988;89: 2763–7. <http://dx.doi.org/10.1063/1.455028>.
- [30] Mies FH. Calculated vibrational transition probabilities of OH ($X^2\Pi$). *J Mol Spectrosc* 1974;53:150–88. [http://dx.doi.org/10.1016/0022-2852\(74\)90125-8](http://dx.doi.org/10.1016/0022-2852(74)90125-8).
- [31] Goldman A, Schoenfeld WG, Goorvitch D, Chackerian Jr C, Dothe H, Mélen F, et al. Updated line parameters for OH $X^2\Pi-X^2\Pi$ ($v'v'$) transitions. *J Quant Spectrosc Radiat Transf* 1998;59: 453–69. [http://dx.doi.org/10.1016/S0022-4073\(97\)00112-X](http://dx.doi.org/10.1016/S0022-4073(97)00112-X).
- [32] Rothman LS, Gordon IE, Babikov Y, Barbe A, ChrisBenner D, Bernath PF, et al. The HITRAN 2012 molecular spectroscopic database. *J Quant Spectrosc Radiat Transf* 2013;130: 4–50. <http://dx.doi.org/10.1016/j.jqsrt.2013.07.002>.
- [33] Rothman LS, Gordon IE, Barber RJ, Dothe H, Gamache RR, Goldman A, et al. HITRAN, the high-temperature molecular spectroscopic database. *J Quant Spectrosc Radiat Transf* 2010;111: 2139–50. <http://dx.doi.org/10.1016/j.jqsrt.2010.05.001>.
- [34] Bernath PF, Colin R. Revised molecular constants and term values for the $X^2\Pi$ and $B^2\Sigma^+$ states of OH. *J Mol Spectrosc* 2009;257: 20–3. <http://dx.doi.org/10.1016/j.jms.2009.06.003>.
- [35] Mélen F, Sauval AJ, Grevesse N, Farmer CB, Servais C, Delbouille L, et al. A new analysis of the OH radical spectrum from solar infrared observations. *J Mol Spectrosc* 1995;174:490–509. <http://dx.doi.org/10.1006/jmsp.1995.0018>.
- [36] Nizkorodov SA, Harper WW, Nesbitt DJ. Fast vibrational relaxation of OH ($v=9$) by ammonia and ozone. *Chem Phys Lett* 2001;341: 107–14. [http://dx.doi.org/10.1016/S0009-2614\(01\)00371-2](http://dx.doi.org/10.1016/S0009-2614(01)00371-2).
- [37] Sappay AD, Copeland RA. Laser double-resonance study of OH ($X^2\Pi$, $v=12$). *J Mol Spectrosc* 1990;143:160–8. [http://dx.doi.org/10.1016/0022-2852\(90\)90267-T](http://dx.doi.org/10.1016/0022-2852(90)90267-T).
- [38] Copeland RA, Chalamala BR, Coxon JA. Laser-induced fluorescence of the $B^2\Sigma^+ - X^2\Pi$ system of OH: molecular constants for $B^2\Sigma^+$ ($v=0, 1$) and $X^2\Pi$ ($v=7-9, 11-13$). *J Mol Spectrosc* 1993;161: 243–52. <http://dx.doi.org/10.1006/jmsp.1993.1229>.
- [39] Abrams MC, Goldman A, Gunson MR, Rinsland CP, Zander R. Observations of the infrared solar spectrum from space by the ATMOS experiment. *App Opt* 1996;35:2747–51. <http://dx.doi.org/10.1364/AO.35.002747>.
- [40] Farmer CB, Norton RH. A high-resolution atlas of the infrared spectrum of the Sun and the Earth atmosphere from space. A compilation of ATMOS spectra of the region from 650 to 4800 cm^{-1} (2.3–16 μm), vol. 1. The Sun. National Aeronautics and Space Administration, Hampton, VA, USA. Langley Research Center; 1989.
- [41] Hardwick JL, Whipple GC. Far infrared emission spectrum of the OH radical. *J Mol Spectrosc* 1991;147:267–73. [http://dx.doi.org/10.1016/0022-2852\(91\)90185-D](http://dx.doi.org/10.1016/0022-2852(91)90185-D).

- [42] Varberg TD, Evenson KM. The rotational spectrum of OH in the $v=0-3$ levels of its ground state. *J Mol Spectrosc* 1993;157: 55–67. <http://dx.doi.org/10.1006/jmsp.1993.1005>.
- [43] Brown JM, Zink LR, Jennings DA, Evenson KM, Hinz A. Laboratory measurement of the rotational spectrum of the OH radical with tunable far-infrared research. *Astrophys J* 1986;307: 410–3. <http://dx.doi.org/10.1086/164427>.
- [44] Davies PB, Hack W, Preuss AW, Temps F. Far infrared laser magnetic resonance spectra of vibrationally excited OH. *Chem Phys Lett* 1979;64:94–7. [http://dx.doi.org/10.1016/0009-2614\(79\)87283-2](http://dx.doi.org/10.1016/0009-2614(79)87283-2).
- [45] Radford HE. Scanning microwave echo box spectrometer 1968;39: 1687–91. <http://dx.doi.org/10.1063/1.1683203>.
- [46] Ball JA, Dickinson DF, Gottlieb CA, Radford HE. The 3.8-cm spectrum of OH: laboratory measurement and low-noise search in W3(OH). *Astronom J* 1970;75:762. <http://dx.doi.org/10.1086/111022>.
- [47] Meerts WL, Dymanus A. A molecular beam electric resonance study of the hyperfine Δ doubling spectrum of OH, OD, SH, and SD. *Can J Phys* 1975;53:2123. <http://dx.doi.org/10.1139/p75-261>.
- [48] Coxon JA, Sastry KVNL, Austin JA, Levy DH. The microwave spectrum of the OH $X^2\Pi$ radical in the ground and vibrationally-excited ($\nu \leq 6$) levels. *Can J Phys* 1979;57:619–34. <http://dx.doi.org/10.1139/p79-089>.
- [49] Destombes JL, Marlière C, Rohart F, Burie J. Nouvelle analyse du spectre Hertzien du radical hydroxyl. *C R Acad Sci B* 1974;278: 275–8.
- [50] Destombes JL, Journel G, Marlière C, Rohart F. Microwave spectrum of hydroxyl radical in $\Pi-2(3/2)$ and $\Pi-2(1)$. *C R Acad Sci B* 1975; 280: 809–11.
- [51] Kolbe WF, Zollner WD, Leskovar B. Microwave spectrometer for the detection of transient gaseous species. *Astrophys J Lett* 1981;52: 523–32. <http://dx.doi.org/10.1063/1.1136633>.
- [52] ter Meulen JJ, Dymanus A. Beam-maser measurements of the ground-state transition frequencies of OH. *Astrophys J Lett* 1972;172:L21. <http://dx.doi.org/10.1086/180882>.
- [53] ter Meulen JJ, Meerts WL, van Mierlo GW, Dymanus A. Observations of population inversion between the Λ -doublet states of OH. *Phys Rev Lett* 1976;36:1031–4. <http://dx.doi.org/10.1103/PhysRevLett.36.1031>.
- [54] Destombes JL, Marlière C. Measurement of hyperfine splitting in the OH radical by a radio-frequency microwave double resonance method. *Chem Phys Lett* 1975;34:532–6. [http://dx.doi.org/10.1016/0009-2614\(75\)85556-4](http://dx.doi.org/10.1016/0009-2614(75)85556-4).
- [55] ter Meulen JJ. Ph.D. thesis. Katholieke Universiteit, Nijmegen, The Netherlands; 1976.
- [56] Meerts WL, Bekooy JP, Dymanus A. Vibrational effects in the hydroxyl radical by molecular beam electric resonance spectroscopy. *Mol Phys* 1979;37:425–39. <http://dx.doi.org/10.1080/00268977900100361>.
- [57] Destombes JL, Lemoine B, Marlière-Demuync C. Microwave spectrum of the hydroxyl radical in the $v=1, ^2\Pi_{3/2}$ state. *Chem Phys Lett* 1979;60:493–5. [http://dx.doi.org/10.1016/0009-2614\(79\)80619-3](http://dx.doi.org/10.1016/0009-2614(79)80619-3).
- [58] Clough PN, Curran AH, Thrush BA. The E.P.R. spectrum of vibrationally excited hydroxyl radicals. *Proc R Soc A* 1971;323: 541–54. <http://dx.doi.org/10.1098/rspa.1971.0122>.
- [59] Lee KP, Tam WG, Larouche R, Woonton GA. Electron resonance of vibrationally excited OH radicals. *Can J Phys* 1971;49: 2207–10. <http://dx.doi.org/10.1139/p71-267>.
- [60] Martin-Drumel MA, Pirali O, Balcon D, Brichignac P, Roy P, Vervloet M. High resolution far-infrared Fourier transform spectroscopy of radicals at the AILES beamline of SOLEIL synchrotron facility. *Rev Sci Inst* 2011;82(11):113106. <http://dx.doi.org/10.1063/1.3660809>.
- [61] van de Meerakker S, Vanhaecke N, van der Loo M, Groenenboom G, Meijer G. Direct measurement of the radiative lifetime of vibrationally excited OH radicals. *Phys Rev Lett* 2005;95: 013003. <http://dx.doi.org/10.1103/PhysRevLett.95.013003>.
- [62] Carleer MR. Wspectra: a Windows program to accurately measure the line intensities of high-resolution Fourier transform spectra. In: Russell JE, Schaefer K, Lado-Bordowsky O, editors. *Remote sensing of clouds and the atmosphere V*, vol. 4168. Society of photo-optical instrumentation engineers (SPIE) conference series; 2001. p. 337–42. <http://dx.doi.org/10.1117/12.413851>.
- [63] Herman R, Wallis RF. Influence of vibration-rotation interaction on line intensities in vibration-rotation bands of diatomic molecules. *J Chem Phys* 1955;23(4):637–46. <http://dx.doi.org/10.1063/1.1742069>.
- [64] Brown J, Carrington A. *Rotational spectroscopy of diatomic molecules*. Cambridge molecular science. Cambridge: Cambridge University Press; 2003.
- [65] Chackerian Jr C, Goorvitch D, Benidar A, Farrenq R, Guelachvili G, Martin PM, et al. Rovibrational intensities and electric dipole moment function of the $X^2\Pi$ hydroxyl radical. *J Quant Spectrosc Radiat Transf* 1992;48: 667–73. [http://dx.doi.org/10.1016/0022-4073\(92\)90130-V](http://dx.doi.org/10.1016/0022-4073(92)90130-V).
- [66] Brown JM, Howard BJ. An approach to the anomalous commutation relations of rotational angular momenta in molecules. *Mol Phys* 1976;31:1517–25. <http://dx.doi.org/10.1080/0026897600101191>.
- [67] Brooke JSA, Bernath PF, Western CM, van Hemert MC, Groenenboom GC. Line strengths of rovibrational and rotational transitions within the $X^3\Sigma^-$ ground state of NH. *J Chem Phys* 2014;141(5): 054310.
- [68] Le Roy RJ. RKR1 2.0: a computer program implementing the first-order RKR method for determining diatomic molecule potential energy functions. University of Waterloo chemical physics research report, University of Waterloo; 2004. <http://www.science2.uwaterloo.ca/~leroy/rkr>.
- [69] Rydberg R. Graphische darstellung einiger bandenspektroskopischer ergebnisse. *Z Phys* 1932;73:376–85. <http://dx.doi.org/10.1007/BF01341146>.
- [70] Rydberg R. Über einige potentialkurven des quecksilberhydrids. *Z Phys* 1933;80:514–24. <http://dx.doi.org/10.1007/BF02057312>.
- [71] Klein O. Zur berechnung von potentialkurven für zweiatomige moleküle mit hilfe von spektraltermen. *Z Phys* 1932;76: 226–35. <http://dx.doi.org/10.1007/BF01341814>.
- [72] Rees ALG. The calculation of potential-energy curves from bandspectroscopic data. *Proc Phys Soc* 1947;59:998–1008. <http://dx.doi.org/10.1088/0959-5309/59/6/310>.
- [73] Werner HJ, Knowles P. A comparison of variational and nonvariational internally contracted multiconfiguration-reference configuration-interaction calculations. *Theor Chem Acc* 1990;78: 175–87. <http://dx.doi.org/10.1007/BF01112867>.
- [74] Gdanitz RJ, Ahlrichs R. The averaged coupled-pair functional (ACPF): a size-extensive modification of MRCI (SD). *Chem Phys Lett* 1988;143: 413–20. [http://dx.doi.org/10.1016/0009-2614\(88\)87388-3](http://dx.doi.org/10.1016/0009-2614(88)87388-3).
- [75] Cave RJ, Davidson ER. Quasidegenerate variational perturbation theory and the calculation of first-order properties from variational perturbation theory wave functions. *J Chem Phys* 1988;89: 6798–814. <http://dx.doi.org/10.1063/1.455354>.
- [76] Szalay PG, Bartlett RJ. Multi-reference averaged quadratic coupled-cluster method: a size-extensive modification of multi-reference CI. *Chem Phys Lett* 1993;214:481–8. [http://dx.doi.org/10.1016/0009-2614\(93\)85670-J](http://dx.doi.org/10.1016/0009-2614(93)85670-J).
- [77] Werner HJ, Knowles PJ, Knizia G, Manby FR, Schütz M, Celani P, et al. MOLPRO, version 2010.1, a package of ab initio programs; 2010. <http://www.molpro.net>.
- [78] Werner HJ, Knowles PJ, Knizia G, Manby FR, Schütz M, Celani P, et al. MOLPRO, version 2012.1, a package of ab initio programs; 2012. <http://www.molpro.net>.
- [79] Dunning Jr. TH. Gaussian basis sets for use in correlated molecular calculations. I. The atoms boron through neon and hydrogen. *J Chem Phys* 1989;90:1007–23. <http://dx.doi.org/10.1063/1.456153>.
- [80] Woon DE, Dunning Jr. TH. Gaussian basis sets for use in correlated molecular calculations. VI. Core-valence basis sets for boron through neon. *J Chem Phys* 1995;103:4572–85. <http://dx.doi.org/10.1063/1.470645>.
- [81] Wilson AK, van Mourik T, Dunning Jr. TH. Gaussian basis sets for use in correlated molecular calculations. VI. Sextuple zeta correlation consistent basis sets for boron through neon. *J Mol Struct: THEOCHEM* 1996;388:339–49. [http://dx.doi.org/10.1016/S0166-1280\(96\)80048-0](http://dx.doi.org/10.1016/S0166-1280(96)80048-0).
- [82] Knowles PJ, Werner HJ. An efficient second-order MC SCF method for long configuration expansions. *Chem Phys Lett* 1985;115(3): 259–567. [http://dx.doi.org/10.1016/0009-2614\(85\)80025-7](http://dx.doi.org/10.1016/0009-2614(85)80025-7).
- [83] Werner HJ, Knowles PJ. A second order multiconfiguration SCF procedure with optimum convergence. *J Chem Phys* 1985;82: 5053–63. <http://dx.doi.org/10.1063/1.448627>.
- [84] Brooke JSA, Ram RS, Western CM, Schwenke DW, Li G, Bernath PF. Einstein A coefficients and oscillator strengths for the $A^2\Pi-X^2\Sigma^+$ (red) and $B^2\Sigma^+-X^2\Sigma^+$ (violet) systems and rovibrational transitions in the $X^2\Sigma^+$ state of CN. *Astrophys J Supp Ser* 2014;210: 23. <http://dx.doi.org/10.1088/0067-0049/210/2/23>.
- [85] Le Roy RJ, Vrsic ER. Periodicity of the oscillatory J dependence of diatomic molecule Franck-Condon factors. *Can J Phys* 1975;53: 1560.
- [86] Larsson M. Conversion formulas between radiative lifetimes and other dynamical variables for spin-allowed electronic transitions in diatomic molecules. *Astron Astrophys* 1983;128:291–8.
- [87] Laraia AL, Gamache RR, Lamouroux J, Gordon IE, Rothman LS. Total internal partition sums to support planetary remote sensing. *Icarus* 2011;215:391–400. <http://dx.doi.org/10.1016/j.icarus.2011.06.004>.
- [88] Drouin BJ. Isotopic spectra of the hydroxyl radical. *J Phys Chem A* 2013;117:10076–91. <http://dx.doi.org/10.1021/jp400923z>.

- [89] Meléndez J. A low solar oxygen abundance from the first-overtone OH lines. *Astrophys J* 2004;615:1042–7. <http://dx.doi.org/10.1086/424591>.
- [90] Kaeufl HU, Ballester P, Biereichel P, Delabre B, Donaldson R, Dorn R, et al. CRIRES: a high-resolution infrared spectrograph for ESO's VLT. In: Moorwood AFM, Iye M, editors. Ground-based instrumentation for astronomy, vol. 5492. Society of photo-optical instrumentation engineers (SPIE) conference series; 2004. p. 1218–27. <http://dx.doi.org/10.1117/12.551480>.
- [91] Wilson JC, Hearty F, Skrutskie MF, Majewski S, Schiavon R, Eisenstein D, et al. The Apache Point Observatory Galactic Evolution Experiment (APOGEE) high-resolution near-infrared multi-object fiber spectrograph. In: Society of photo-optical instrumentation engineers (SPIE) conference series, vol. 7735; 2010. p. 1. <http://dx.doi.org/10.1117/12.856708>.
- [92] Park C, Jaffe DT, Yuk IS, Chun MY, Pak S, Kim KM, et al. Design and early performance of IGRINS (immersion grating infrared spectrometer). In: Society of photo-optical instrumentation engineers (SPIE) conference series, vol. 9147; 2014. p. 1. <http://dx.doi.org/10.1117/12.2056431>.
- [93] Asplund M, Grevesse N, Sauval AJ, Allende Prieto C, Kiselman D. Line formation in solar granulation. IV. [O I], O I and OH lines and the photospheric O abundance. *Astron Astrophys* 2004;417:751–68. <http://dx.doi.org/10.1051/0004-6361:20034328>.
- [94] Hinkle KH, Wallace L, Ram RS, Bernath PF, Sneden C, Lucatello S. The magnesium isotopologues of MgH in the $A^2\Pi-X^2\Sigma^+$ system. *Astrophys J Suppl* 2013; 207: 26. <http://dx.doi.org/10.1088/0067-0049/207/2/26>.
- [95] Ram RS, Brooke JS, Bernath PF, Sneden C, Lucatello S. Improved line data for the Swan system $^{12}\text{C}^{13}\text{C}$ isotopologue. *Astrophys J Suppl* 2014;211:5. <http://dx.doi.org/10.1088/0067-0049/211/1/5>.
- [96] Sneden C, Lucatello S, Ram RS, Brooke JS, Bernath P. Line lists for the $A^2\Pi-X^2\Sigma^+$ (red) and $B^2\Sigma^+-X^2\Sigma^+$ (violet) systems of CN, $^{13}\text{C}^{14}\text{N}$, and $^{12}\text{C}^{15}\text{N}$, and application to astronomical spectra. *Astrophys J Suppl* 2014; 214: 26. <http://dx.doi.org/10.1088/0067-0049/214/2/26>.
- [97] Sneden C. The nitrogen abundance of the very metal-poor star HD 122563. *Astrophys J* 1973;184:839–49. <http://dx.doi.org/10.1086/152374>.
- [98] Kurucz RL. Including all the lines. *Can J Phys* 2011;89:417–28. <http://dx.doi.org/10.1139/p10-104>.
- [99] Lawler JE, Wood MP, Den Hartog EA, Feigenson T, Sneden C, Cowan JJ. Improved $V\log(gf)$ values and abundance determinations in the photospheres of the Sun and metal-poor star HD 84937. *Astrophys J Suppl* 2014;215:20. <http://dx.doi.org/10.1088/0067-0049/215/2/20>.
- [100] Sneden C, Lawler JE, Cowan JJ, Ivans II, Den Hartog EA. New rare earth element abundance distributions for the sun and five r-process-rich very metal-poor stars. *Astrophys J Suppl* 2009;182:80–96. <http://dx.doi.org/10.1088/0067-0049/182/1/80>.
- [101] Asplund M, Grevesse N, Sauval AJ, Scott P. The chemical composition of the Sun. *Annu Rev Astron Astrophys* 2009;47:481–522. <http://dx.doi.org/10.1146/annurev.astro.46.060407.145222>.
- [102] Holweger H, Müller EA. The photospheric barium spectrum – solar abundance and collision broadening of BA II lines by hydrogen. *Sol Phys* 1974; 39: 19–30. <http://dx.doi.org/10.1007/BF00154968>.
- [103] Hinkle K, Wallace L, Valenti J, Harmer D. Visible and near infrared atlas of the Arcturus spectrum 3727–9300 Å. Astronomical Society of the Pacific Monograph Publications, San Francisco; 2000.
- [104] Allende Prieto C, Majewski SR, Schiavon R, Cunha K, Frinchaboy P, Holtzman J, et al. APOGEE: the Apache point observatory galactic evolution experiment. *Astronom Nachr* 2008;329:1018. <http://dx.doi.org/10.1002/asna.200811080>.
- [105] Ramírez I, Allende Prieto C. Fundamental parameters and chemical composition of Arcturus. *Astrophys J* 2011;743:135. <http://dx.doi.org/10.1088/0004-637X/743/2/135>.
- [106] Brooke JS, Bernath PF, Western CM. Improved line strengths of rovibrational and rotational transitions within the $X^3\Sigma^-$ ground state of NH. *J Chem Phys* 2015;143:026101. <http://dx.doi.org/10.1063/1.4923422>.